(This is a sample cover image for this issue. The actual cover is not yet available at this time.)

Comput. Methods Appl. Mech. Engrg. 223–224 (2012) 103–122

Contents lists available at SciVerse ScienceDirect

Comput. Methods Appl. Mech. Engrg.

journal homepage: www.elsevier.com/locate/cma

A unified level set based methodology for fast generation of complex microstructural multi-phase RVEs

B. Sonon, B. François, T.J. Massart *

Université Libre de Bruxelles (ULB), Building, Architecture & Town Planning Dept. (BATir) CP 194/02, Avenue F.D. Roosevelt 50, 1050 Bruxelles, Belgium

ARTICLE INFO

Article history:
Received 1 September 2011
Received in revised form 10 February 2012
Accepted 23 February 2012
Available online 3 March 2012

Keywords:
Computational microstructure generation
Level set functions
Random Sequential Addition
Computational homogenization
Particulate media
Polycrystalline aggregates

ABSTRACT

In the frame of the multi-scale computational analysis of complex materials, the generation of Representative Volume Elements (RVE) is often a crucial step. Various microstructure generation tools may be used, depending on the material to be considered, such as Discrete Element Methods (DEM), Random Sequential Addition (RSA) based methods for particulate media requiring important computation times; or Voronoï tessellation methods for polycrystalline materials. Besides being material specific, some of these methods may become unaffordable when considering complex microstructures, large inclusions numbers or high volume fractions. The present contribution presents a unified level set based methodology for complex, periodic (or not) and random RVE generations. The presented methodology allows RVE generation for particulate granular media, polycrystalline aggregates with large size distribution and arbitrary shapes, as well as for complex three-phase or poly-phase microstructures. A level set controlled Random Sequential Addition algorithm is used for particle distribution generation, allowing increasing the RSA algorithm efficiency, generating large and dense populations of arbitrary shaped inclusions with precise control on neighboring distances. Starting from this, several methods are presented to add specific realistic features to the generated RVEs. Modifications and densifications allow the distribution pattern to fit observed real samples or to present a specific spatial organization. The addition of one (or more) phase(s) obtained from the growth of the initial inclusions allows reproducing some typical microstructural patterns such as grain bridging in clayey soils, interfacial transition zones in concrete or hydrated gel in cement paste. The versatility of the proposed RVE generation method is illustrated by means of various examples, reproducing realistic microstructural arrangements of clayey soils, irregular masonry and polycrystalline aggregates with bimodal size distributions.

1. Introduction

1.1. Context

Computational homogenization techniques have been used extensively over the last two decades to link the overall properties of materials to their internal structure. While homogenization methods started from closed-form or semi-analytical procedures [59], or asymptotic homogenization methods [65,39]; a large number of contributions deals with the computational homogenization of materials [88,33,34,22,55,74,83]. Computational homogenization is usually employed with various objectives when the problem becomes too complex to derive closed-form solutions. The objective can either consist of identifying the microstructural process responsible for a macroscopic effect, or of obtaining average macroscopic properties based on the material properties of constituents. Some references are related to periodic materials such as masonry [40–42] or make the assumption of a simplified version of the microstructure with respect to reality for a large number of materials such as polymers [88], soils [7], rocks [20] or metals [44,19], in which case the complexity originates from the evolving non linear behavior of constituents. The complexity of the overall response of a heterogeneous material may also stem from the complexity of its fabric. Other works have examined complex microstructures such as concrete [31,63], particulate frictional media without cohesion [91,47,5], bimodal polycrystalline structures [43], irregular masonry [49,94,37], or wood [60]. For such complex and apparently random microstructures, contributions also intended to quantify the overall uncertainty on the macroscopic behavior related to the observed variability at the fine scale through computational homogenization techniques [27,49].

If the complex behavior of some materials at the macroscopic scale originates from a complex organization of phases with a simpler behavior at the microscopic scale, using geometrically over simplified Representative Volume Elements (RVEs) for homogenization may lead to wrong conclusions with respect to the dominant microstructural mechanisms. In most of these examples, a crucial step

* Corresponding author.
E-mail address: thmassar@batir.ulb.ac.be (T.J. Massart).

0045-7825/$ - see front matter © 2012 Elsevier B.V. All rights reserved.
http://dx.doi.org/10.1016/j.cma.2012.02.018

therefore consists in generating RVEs matching the available experimental data, such as for instance the volume fractions of the phases, the experimentally obtained size distribution of inclusions and/or voids, or the amount of binding phase between particles if any.

1.2. RVE acquisition methods

Several RVE generation methodologies for random materials were proposed previously. They are usually specific to the type of materials, i.e. Random Sequential Addition (RSA) or Discrete Element Method (DEM) for particulate media, and Voronoï tessellation methods for polycrystals. A complete state of the art for particulate media RVE generation can be found in [25].

RSA can be used to generate an arbitrary arrangement of inclusions in a given RVE size [72,82,12]. It is the simplest methods for generation of RVEs containing a low density of inclusions approximated by circles or spheres. However, the performance of RSA depends almost exponentially on the targeted density, and any improvement such as accommodating arbitrary shaped inclusions or controlling neighboring distances dramatically affects the efficiency of the addition process. Note however that RSA is often the only way to give an input for dynamic methods and is widely used in this purpose.

Dynamic methods for particles packing have been introduced in [29,30,92,21,73] based on simplified version of DEM [13–15], thereby allowing particle rearrangements and reaching higher densities. This also allows providing movement and contact laws to govern the particles interactions during the simulated mixing/compaction process. This approach was applied with success to model concrete [77,78,75,76,26], soil or other particulate media [13]. It involves a rather important computational effort, but carries the advantage to incorporate physically based modeling for "manufactured" microstructures. In some instances however as is the case for soils, it is not required to reproduce a mixing process to obtain the initial fabric of the material, and the number of small particles to consider may render a DEM based compaction unaffordable. Furthermore, the distinction between voids and a third (binding) phase in the RVE is also more difficult to accommodate with DEM based approaches.

Some intermediate methods have also be proposed as in [11,95]. In [4], circular inclusions are randomly placed and subsequently moved to optimize the spatial organization. In [10], purely geometrical methods are used to pack a given set of arbitrary shaped inclusions.

Conversely, polycrystalline RVEs are usually obtained based on *Voronoï tessellation methods* [66,67,86,64], which is very effective in generating grains assemblies based on a random distribution of points. However, managing more complex features such as precise bimodal distributions of grain sizes can be difficult and may lead to complex iterative procedures. Moreover, these methods can only produce convex grain shapes while real microstructures may require non convex shapes.

Except for granular materials with circular/spherical grain shapes for which existing methods are effective, there is a need for *fast and easy RVE generation* if one desires to investigate macroscopic effects of microstructural variability for a given material. Few methods actually exist for the generation of RVEs of more complex materials in which a third phase is present such as clayey sand (binding clay material between sandy rigid particles and voids). Highly bi-modal polycrystalline pattern are also difficult to obtain in a fast and efficient way.

1.3. Paper outline

The present contribution deals with a *unified level set based methodology*, able to generate different types of microstructures (particulate media or polycrystalline aggregates) with no convexity restriction on particle shapes and allowing the incorporation of a third specific phase in a consistent way with specific fabric patterns. The presented RVE generation method consists of three tools.

- *A random inclusion distribution generator*, in which the use of a simple level set control allows the efficient exploitation of the simplest RSA algorithm. It constitutes the starting basis for the overall methodology. The level set control allows a fast sequential addition algorithm to treat large and dense distributions of several populations of arbitrary shaped inclusions, accommodating prescribed particle size distributions with a strong repeatability and adaptivity.
- *A new morphing tool* allows modifying/densifying/complexifying the starting distribution, based on isocontour curves of level set functions constructed with signed distance functions of the initially generated inclusions, and used to define new curves for morphed inclusions. This allows achieving several specific pattern such as very dense rock arrangements, polycrystalline aggregates and other features with a very limited computing cost.
- Using level set functions, *the incorporation of a third phase* is finally obtained, based on the initially generated inclusions. This allows reproducing specific fabric patterns such as bridging, coating, layering or the presence of micro-cracks and voids.

It is emphasized that microstructural features generated by the proposed methodology are not derived from the physical modeling of their formation processes. Observations and measurements on real samples as well as the expertise related to the concerned material are therefore required to generate proper RVEs. The particular case of micro-cracks described here therefore relates to the incorporation of initial observable micro-cracks in the microstructure.

The paper is structured as follows. Section 2 shortly introduces level set functions and emphasizes the main formalism used for the presented methodology. Section 3 describes the random inclusion distribution generator. Based on the most simple RSA algorithm that will be introduced first, the level set controlled RSA is explained and its ability to efficiently produce RVEs with prescribed particle distributions is demonstrated. In particular, the linearity of the generation computational cost with respect to the number of added inclusions is illustrated, as well as the efficiency for dealing with complex arbitrary shaped inclusions and with precise control on neighboring distances. Section 4 describes both tools allowing specific operations on an inclusion distribution based on isocontour curves of specific level set functions to define specific features in the generated RVE. These tools appear to be versatile and adaptable without any heavy computational operation. Section 5 applies the proposed concepts to three different illustrative applications. First, RVEs matching realistic particle size distributions of a clayey soil are presented. The second example consists of polycrystalline aggregates with bimodal grain size distribution, while an irregular masonry mesostructure is considered as a third example. Section 6 discusses the results and potential further improvements of the framework, before conclusions are drawn in Section 7.

All the presented concepts are valid in 2 or 3 dimensions. They are presented and implemented here in a 2D setting for the sake of illustration, and without loss of generalization to three-dimensional cases.

In the sequel of the paper, the term "particle" will refer here to *physical particles* such as sand grains or rock fragments in concrete. The term "inclusion" will be used with a *geometrical meaning*, referring to any closed curve defining an inclusion in a continuous

"matrix", irrespective of their physical nature (e.g. for porous concrete we will speak about "void inclusions in a matrix of cement paste", dry sand may be described as "a particle inclusion assembly in a void matrix").

2. Level set functions

2.1. Level set for a single inclusion

Level set functions were originally introduced in computational methods to model propagating fronts described by the Hamilton–Jacobi equation [57,56,71,70,2,17]. Level set tools have since then been used in other contexts as a general tool to handle complex or evolving geometries. They are widely used in medical imaging [8,79], in image analysis [38,93], in tomography to generate "exact" 3D geometrical data set from scanned object [28,35], in topological optimization to follow the evolution of a trial geometry [90] and in XFEM approaches using the concept of partition of unity to handle complex microstructures including many material interfaces without meshing difficulties [80,51,18,23,24,85,35].

The concept of level set originates from the idea of defining implicitly a curve (resp. surface) Φ by the iso-contour (resp. iso-surface) of a 2D (resp. 3D) function with $\Phi \equiv \mathrm{LS}(\mathbf{x},\ldots) = k$. The *level set function* $\mathrm{LS}(\mathbf{x},\ldots)$ can be of different nature and may depend on various parameters. A particular choice for this function is the signed distance to Φ because in addition to define implicitly a curve, it also gives local information about distances from the curve and direction or curvature of the curve. A natural governing parameter of this function may be time, in order to describe implicitly the motion of a curve through a time dependent level set function. In this paper, we will use level set functions some of them not being signed distance functions. The additional parameters governing $\mathrm{LS}(\mathbf{x},\ldots)$, if any, will be based not on time but on microstructural features descriptors. The starting step for the evaluation of the different level set functions that will be used is the signed distance from single inclusions or features present in the RVE. Those starting level set functions are then pure static distance fields but the term *level set function of* Φ (or simply *level set of* Φ) will be used in the sequel of this paper to denote this particular function. Other level set functions will receive specific names or will be denoted directly by their symbol.

Given an interface Φ dividing the RVE domain Ω in two sub-domains Ω^+ and Ω^-, *the level set of* Φ is a function $\mathrm{LS}_\Phi(\mathbf{x})$ of space coordinates $\mathbf{x}$ with the value of the signed distance from $\mathbf{x}$ to Φ. The sign of the function depends whether $\mathbf{x}$ lies in Ω^+ or Ω^-. If Φ is closed (i.e. if the interface describes an *inclusion*), Ω^- will be by convention the included sub-domain. The level set functions of inclusions in the RVE could therefore be used also to characterize point-to-inclusion distances, any negative value reflecting a position occupied by an inclusion.

The equation giving the value of $\mathrm{LS}_\Phi(\mathbf{x})$ depends on the shape of the inclusion boundary Φ. For example the level set for a circular interface of center $\mathbf{x}_c$ and radius r is given by

$$\mathrm{LS}_\Phi(\mathbf{x}) = ||\mathbf{x} - \mathbf{x}_c|| - r. \tag{1}$$

A fast scheme to compute level set functions for convex or concave 2D polygonal inclusions is given in Appendix A.1. Fig. 1 illustrates the level set function of such an inclusion.

2.2. Global level set for microstructures

In the context of microstructural RVE generation, a large number of inclusions need to be incorporated and *global distance functions* can be used to define a global descriptor of the microstructure geometry. Considering a set of inclusions Φ_i in the RVE domain

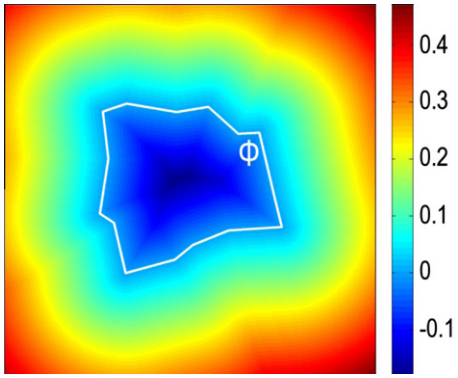

Fig. 1. Level set of a polygonal inclusion. Distances are measured in relative unit (RVE size = 1), a convention used in the sequel of the paper.

with $i \in \mathbf{I}$ subset of $\mathbf{N}$ indexing inclusions, the *first nearest neighbor distance function*, denoted here LS_1 can be defined as follows, see Fig. 2

$$\mathrm{LS}_1(\mathbf{x}) = \min_i[\mathrm{LS}_{\Phi i}(\mathbf{x})]. \tag{2}$$

The *second nearest neighbor distance function*, denoted here LS_2 can also be evaluated. During the evaluation of (2), it is possible (and computationally free) to construct $\mathbf{J}(\mathbf{x})$, the set of inclusion indexes $\mathbf{I}$ except the one which satisfy (2) for a given $\mathbf{x}$ and hence compute $\mathrm{LS}_2(\mathbf{x})$ according to the following relations with $j \in \mathbf{J}(\mathbf{x})$, see Fig. 3

$$\mathbf{J}(\mathbf{x}) = \mathbf{I} \setminus \operatorname*{argmin}_i[\mathrm{LS}_{\Phi i}(\mathbf{x})], \tag{3}$$

$$\mathrm{LS}_2(\mathbf{x}) = \min_j[\mathrm{LS}_{\Phi j}(\mathbf{x})]. \tag{4}$$

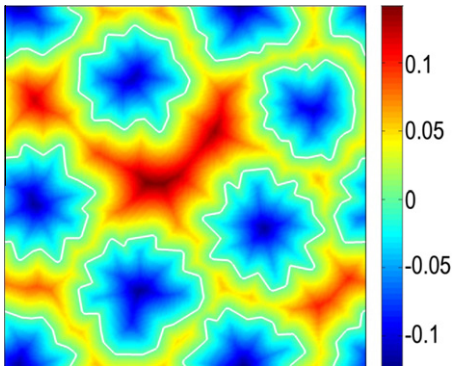

Fig. 2. Plot of function $\mathrm{LS}_1(\mathbf{x})$ for a given microstructure (white lines denote boundaries of inclusions).

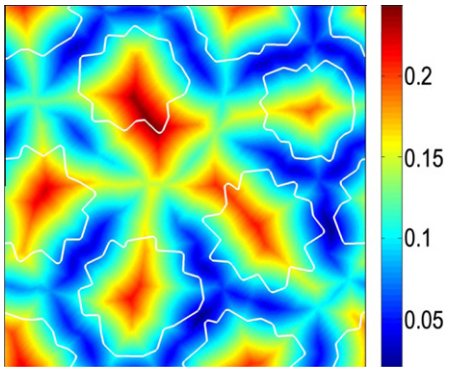

Fig. 3. Plot of function $\mathrm{LS}_2(\mathbf{x})$ for a given microstructure (white lines denote boundaries of inclusions).

$LS_1(\mathbf{x})$ and $LS_2(\mathbf{x})$ are piecewise equal to i functions $LS_{\Phi i}(\mathbf{x})$ and therefore inherit (everywhere but at the inclusion domains of influence boundaries) from the same properties as signed distance functions, i.e.:

- The norm of the gradient of these functions is almost everywhere equal to 1.
- The direction of the gradient of $LS_1(\mathbf{x})$ (resp. $LS_2(\mathbf{x})$) is almost everywhere normal to the nearest (resp. second nearest) curve.

$LS_1(\mathbf{x})$ can be used strictly as a level set function to define implicitly every inclusion boundary inside the RVE with a single function. $LS_2(\mathbf{x})$ is not associated with any interface in particular and will not be used strictly as a level set in the method. However, this function can be used to measure inclusion-to-inclusion distances with a direct interpretation of definitions (3) and (4): For every $\mathbf{x}$ on the RVE domain satisfying $LS_{\Phi i}(\mathbf{x}) = 0$ for a given i, $LS_2(\mathbf{x})$ is equal the minimum distance from $\mathbf{x}$ on Φ_i to any other inclusion. This point of view has already been used for contact detection problems in [73] for a DEM-type algorithm, and will again be used here to generate microstructural features depending on inclusion-to-inclusion distances.

2.3. Sequential level set evaluation for microstructures

In a computational context, functions $LS_{\Phi i}(\mathbf{x})$, $LS_1(\mathbf{x})$ and $LS_2(\mathbf{x})$ will be evaluated for a discrete set of $\mathbf{x}_n$ points inside the RVE. Any operation applied on this set of discrete evaluation points $y = f(\mathbf{x}_n)$ may therefore be vectorized. Note that this set should be adapted to the inclusion population considered. Depending on the discretisation size h used for the evaluation of $LS_1(\mathbf{x})$, two or more inclusions closer than h will not be properly resolved and will merge on a short distance (relative to h). Most RVEs shown in this paper have been generated with a 100×100 regular grid for $\mathbf{x}_n$. Some larger RVEs required finer grids of 200×200 points and are identified by the words "double precision" in the related figure captions. Finer grid can be used to produce very detailed RVEs. However, the reader should be aware that too detailed RVEs may lead to heavy computation times in subsequent uses of RVEs in physical simulations. For RVE generation based on sequential addition, it is also convenient to build these functions sequentially, for each new inclusion Φ added in the RVE at a time t based on the previous value of $LS_1(\mathbf{x}_n)^{t-1}$, $LS_2(\mathbf{x}_n)^{t-1}$ and $LS_\Phi(\mathbf{x}_n)^t$ of the new inclusion.

The rules to sequentially evaluate first and second neighbor distance functions (denoted in the sequel "sequential level set refreshing rules") can easily be derived from the definitions as

$$LS_1(\mathbf{x}_n)^t = \min[LS_1(\mathbf{x}_n)^{t-1}, LS_\Phi(\mathbf{x}_n)^t], \tag{5}$$

$$LS_2(\mathbf{x}_n)^t = \max[LS_1(\mathbf{x}_n)^{t-1}, \min[LS_2(\mathbf{x}_n)^{t-1}, LS_\Phi(\mathbf{x}_n)^t]]. \tag{6}$$

Furthermore, the cost of this operation can be dramatically reduced by performing each sequential level set refreshing in two step. During the first step, operations (5) and (6) are performed with the level set of the Smallest Enclosing Circle (SEC) to the newly added inclusion Φ with (1) which is computationally cheap, saving new computed values temporarily. Every $\mathbf{x}_i$ for which the temporary LS_1^t or LS_2^t values are different from LS_1^{t-1} and LS_2^{t-1} are marked as belonging to the maximum influence sub-domain of Φ, see Fig. 4b. This sub-domain depends on the average size of the inclusion and on the density of inclusions already mapped in LS_1^{t-1} and LS_2^{t-1}. In a second step, real values of $LS_\Phi(\mathbf{x}_i)^t$ are evaluated, which may be computationally relatively heavier for complex shapes, but is performed only on the selected sub-domain to achieve the refreshing, see Fig. 4c.

This operation will be denoted "adaptive level set refreshing". Its influence on the resulting performance of the addition process will be discussed further in Section 3.3.

2.4. Periodicity consideration

When generating RVEs for physical multi-scale modeling, it is often required to enforce periodic boundary conditions at the RVE boundaries. Therefore, the LS_1 and LS_2 functions introduced before also have to be periodic. Since these functions are distance functions, inclusions entirely out of the RVE (periodic neighbor of inclusions located entirely in the RVE near a boundary) can however add a contribution inside the RVE near boundaries. This occurs when such a periodic neighbor is nearer from a boundary than the nearest inclusion in the RVE. Actually, in the general 2D case, 3 of the 8 periodic neighbors of an inclusion are susceptible to have a part of their influence domain in the RVE, see Fig. 5a. Due to this, to enforce periodicity, each inclusion, intersecting the boundary or not, has to be accompanied with 3 periodic neighbor inclusions and 3 additional $LS_{\Phi n}(\mathbf{x}_i)$ have to be evaluated on the RVE domain to perform a proper refreshing. Even though this may appear heavy for complex inclusion shapes, adaptive refreshing will be shown to restrict the computational cost to the same as that for non-periodic generations. The 3 periodic neighbors of a given inclusion can be defined by 3 translations $\mathbf{t}_p$, and the associated 3 periodic $LS_{\Phi p}(\mathbf{x}_n)$ can be evaluated from $LS_\Phi(\mathbf{x}_n)$ according to

$$LS_{\Phi p}(\mathbf{x}_n) = LS_\Phi(\mathbf{x}_n - \mathbf{t}_p) \tag{7}$$

When using the above-mentioned adaptive refreshing, the domain of influence in the RVE of the 3 relevant periodic neighbors (red area on Fig. 5b) can be predicted with the SEC of these 3 inclusions. Using the above translation rules, the level set of the original inclusion in domains outside the RVE (blue domains in Fig. 5b) are used to perform the refreshing. The computational cost is then the same as without periodicity, only the level set of the SEC of the inclusion

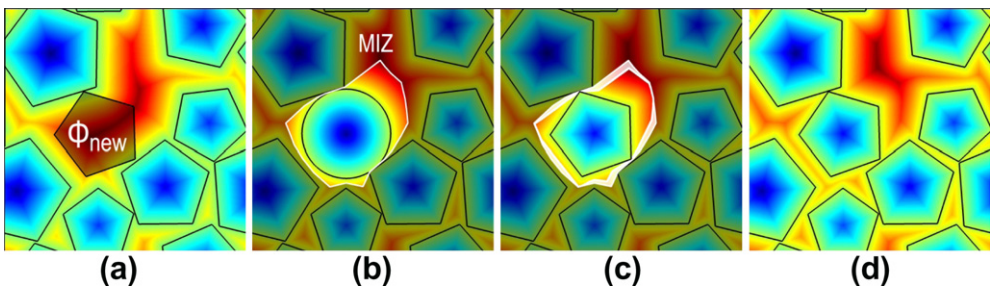

Fig. 4. Adaptive level set refreshing. (a) Plot of $LS_1(\mathbf{x})$ that has to be updated. The shaded inclusion Φ_{new} is the new inclusion to incorporate. (b) Level set function of the SEC of Φ_{new} is evaluated on the entire RVE and minimized with $LS_1(\mathbf{x})$ to find the maximal influence zone (MIZ) of Φ_{new}. The shaded area will not be influenced by Φ_{new} as points belonging to it are closer to other inclusions than to the SEC of Φ_{new}. (c) Level set of Φ_{new} is evaluated only on the MIZ. Points $\mathbf{x}$ lying in the bright area are closer to the SEC of Φ_{new} than to other inclusions but are closer to an inclusion Φ_i than to Φ_{new}. This area is small which leads to good computational efficiency. (d) Level set of Φ_{new} is minimized by $LS_1(\mathbf{x})$ and $LS_1(\mathbf{x})$ is finally updated with those values.

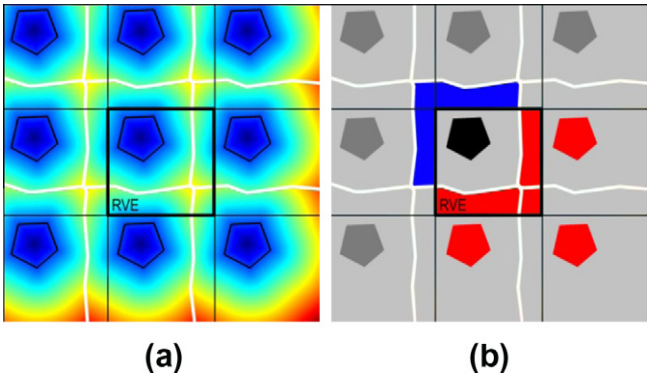

Fig. 5. Periodicity handle. (a) $LS_1(\mathbf{x})$ of an inclusion and its eight periodic neighbors. White lines are the boundaries of influence domains of inclusions. (b) Using adaptive refreshing, periodicity is treated by extending the influence domain out of the RVE (blue domains) and by bringing them back in the RVE to its periodic location (red domains) with translations. (For interpretation of the references to color in this figure legend, the reader is referred to the web version of this article.)

has to be evaluated four times, which is not computationally costly. Fig. 5 illustrates the case of the first inclusion. For every subsequent refreshing, the influence domain of periodic neighbors (red domains in Fig. 5b) is limited by the previously added inclusions and these domains may vanish for a large number of inclusions.

2.5. Inclusion shape modification with offsets

If we assume from now that any curve will be implicitly described with its associated level set function, this function can then be directly used to modify the associated inclusion shape. A simple example of inclusion growth is illustrated here that will be used in further developments. Other possibilities offered by this manipulation are extensively described in [32,56,71].

The "growth" or "shrinking" of inclusions can be used for various reasons. First, this may be seen as a convenient way to adjust the volume fraction reached for a given inclusion distribution. Second, this may be a way to mimic a process of microstructural formation. Finally, it allows transforming polygons into rounded equivalents inclusions if needed depending on the observed features on real sample (e.g. by experimental observation).

An offset of displacement d from an interface Φ is the curve materializing the locus of points located at a distance d from the original interface, see Fig. 6a. In a level set context, if Φ is defined by the iso-zero curve of $LS_\Phi(\mathbf{x})$, any offset of displacement d for this inclusion can be performed by extracting a new curve from the iso-zero curve of $LS_\Phi(\mathbf{x}) - d$. Since the explicit definition of the curve is not used (except for plots) but rather the level set associated with it, this can directly be performed by modifying the level set definition for an inclusion by adding an offset term

$$LS_{\Phi\text{offset}}(\mathbf{x}) = LS_\Phi(\mathbf{x}) - d. \tag{8}$$

This feature can also be used to produce multi-layered inclusions such as particles in concrete surrounded by an Interfacial Transition Zone (ITZ), clay platelets surrounded by adsorbed water or more complex features present in organic microstructures. Rounded and/or layered inclusion interfaces can then be manipulated as efficiently as the original polygonal inclusions, with the related offset values as the additional data to use. A global offset may indeed be performed directly on LS_1 if there is a need of inclusion growing and coalescence. Any inclusion overlap caused by an offset larger than the initial inter inclusion distance will cause separate boundaries to collapse in a single curve, a feature which can be required for particular microstructures (e.g. hydrated cement gel at very fine scale).

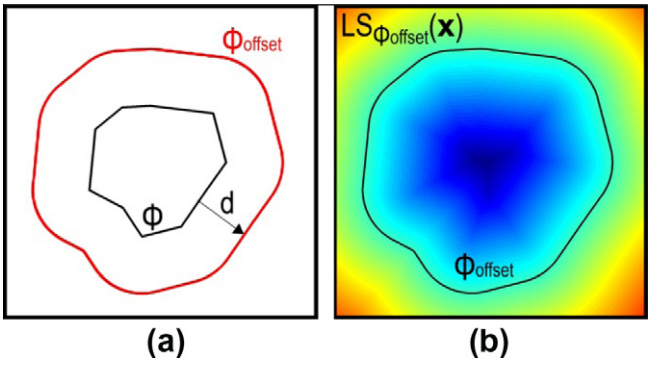

Fig. 6. Inclusion offset. (a) Offset definition (b) Level set of the resulting inclusion.

3. Random inclusion distribution generator

3.1. Classical Random Sequential Addition (RSA)

The classical RSA algorithm is briefly described now as a basis for RVE generation with its main advantages and weaknesses. The principle of the RSA methodology consists in filling the RVE container with inclusions of a given size distribution. These inclusions are sequentially placed at random positions, while enforcing that no overlapping exists with the previously added inclusions. Any overlap leads to a rejection and to a new position generation [72,82,12]. Inclusion-to-inclusion distances rejecting criteria can also be added (see feature (b) below). The verification that the criterion is satisfied or not is called here the "tests".

The following general rules of sequential addition for inclusion distribution generation are common to most RSA approaches and are more specifically discussed in [25]. (a) Large inclusions must be generated first to avoid a dilute distribution of small inclusions leaving no free area large enough to put larger inclusions even if the global volume fraction seems to allow it. (b) To achieve high density, it is advisable to add new inclusions as close as possible from previously added ones to optimize the spatial organization required for dense packing. This can be achieved by imposing rules on distances from each new inclusion to the previously added ones (e.g. to the nearest and/or second nearest neighbor inclusion). Such rules can also be used to control the global pattern of the microstructure as they comply with observations on real specimens and may have a major influence on physical phenomena [84]. (c) Periodicity (in addition to be well appreciated for multi-scale modeling) increases the density that can be reached, due to the suppression of the "boundary effect" which can decrease locally the density.

For the sake of comparisons, the simplest RSA, denoted here as the classical RSA, will be used even though some improvements were already suggested by some authors (e.g. [4]). Any improvements previously proposed are still relevant and may fruitfully be combined with the level set methodology proposed hereafter as well.

In the classical RSA algorithm, the costly operation is the inclusion-to-inclusion distances evaluation step to perform overlap and neighboring *tests*. Since these operations have to be performed for each trial position for a inclusion, the computational cost of the classical RSA is not directly proportional to the target density or number of inclusions, but strongly depends on the success probability of the tests. Since this probability dramatically decreases during the RVE filling, the computational cost increases exponentially with the targeted density as illustrated in Fig. 7 and in [82,25].

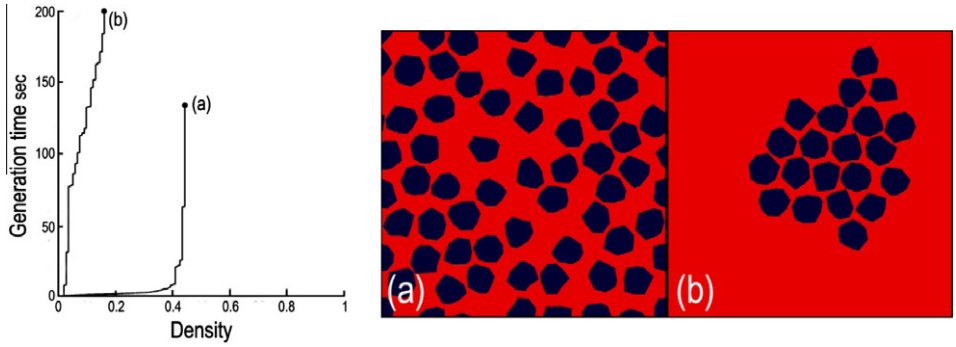

Fig. 7. Generation time against density for classical RSA. (a) Non-overlap control only and (b) enforcing a maximal neighboring distance.

With non-overlap control only, the computation time is increasing with the density due to the free area decrease. The maximum reachable density is quite low. Enforcing a maximal distance between inclusions to optimize the spatial organization theoretically increases the density but the time required to fill the RVE becomes unacceptable, see Fig. 7.

3.2. Level set controlled RSA (LS-RSA)

In order to overcome the main drawback of the RSA (i.e. the increase of the rejection rate of the inclusion potential position to prevent overlapping when the volume fraction increases and/or if a need of neighboring control lead to very restrictive *tests*), we present here a level set control, denoted *LS finder*. It allows preventing any rejection by restricting the random position for a new inclusion to be chosen in sub-domains of the RVE where it is known *a priori* that this inclusion will respect all the criteria of the *tests*. For a given inclusion, the *LS finder* will select in a large set of discrete structured or unstructured positions in the RVE discretizing the description of the LS functions those which satisfy the non-overlapping criterion and/or specification in terms of maximum neighboring distances. This can easily be achieved with logical operations on the $LS_1(\mathbf{x})$ and $LS_2(\mathbf{x})$ functions defined previously.

For example, an inclusion of SEC of radius r will not overlap any inclusion in the RVE already mapped in $LS_1(\mathbf{x})$ if the center of its SEC $\mathbf{x}_c$ satisfies the condition

$$LS_1(\mathbf{x}_c) > r \tag{9}$$

The use of condition (9) is illustrated in Fig. 8b. To achieve higher densities, a control on maximum distances from the first and/or second nearest neighbors (denoted nnl1 and nnl2 in the sequel) can help producing closer packages. The conditions for such a distance control can be written in terms of LS_1 and LS_2 as

$$LS_1(\mathbf{x}_c) < \text{nnl1} + r, \tag{10}$$

$$LS_2(\mathbf{x}_c) < \text{nnl2} + \text{r}. \tag{11}$$

The use of relation (9)–(11) is illustrated in Figs. 8 and 9.

With such simple conditions, the LS-RSA algorithm can be reformulated as follows:

Construct a (un)regular grid of $\mathbf{x}_n \in$ RVE and initialize $LS_1(\mathbf{x}_n)$ and $LS_2(\mathbf{x}_n)$ to $+\infty$ at these points. Loop the following steps until the RVE is full or until the desired density is reached:

- Generate or pick a trial inclusion from a parametric random definition or a predefined set (polygonal, ...), with respect to a prescribed size distribution function.
- Perform operation (9) to simply avoid overlapping, completed with (10) and/or (11) if specifications on neighboring distances are desired, and retain the satisfying positions $\mathbf{x}_c$. Choose randomly in this set a position for the new inclusion. If the retained set is empty, the RVE is full (no inclusion can be added respecting the criteria), then skip the next step and end the loop.
- Refresh $LS_1(\mathbf{x}_n)$ using sequential refreshing rules (see Section 2.3), evaluating $LS_\Phi(\mathbf{x}_n)$ of the new inclusion while respecting the adaptive scheme presented above.

It is emphasized that this procedure allows incorporating an experimentally measured size distribution function as will be demonstrated in Section 5 related to applications.

Note that if it is desired to prevent inclusions to intersect the RVE boundaries, $LS_1(\mathbf{x}_n)$ must be initialized with the (positive) distances from $\mathbf{x}_n$ to the nearest boundary instead of $+\infty$. Then, the *finder* will automatically exclude positions leading to inclusion intersections with boundaries, as illustrated in Fig. 10. Note that any shape can be used as a container instead of a square box, initializing $LS_1(\mathbf{x}_n)$ to the inverted (positive inside) level set of this shape rather than to the distance to the box boundary.

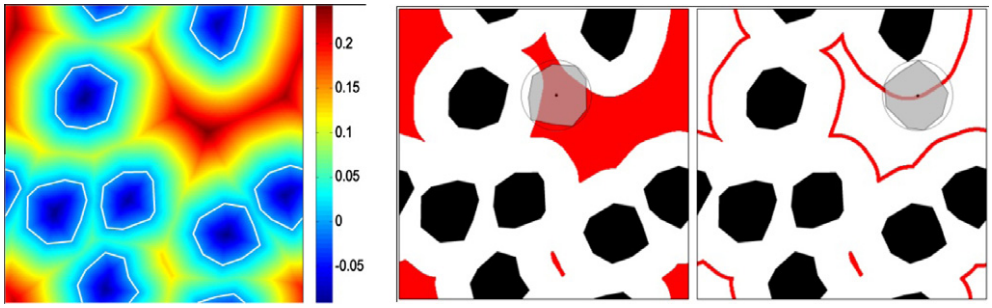

Fig. 8. Level set finder using LS_1. The red points denote positions where the imposed conditions are satisfied. The next inclusion to add (the gray one in its SEC) can be randomly placed on any of these points to fulfill the imposed criteria. (left) $LS_1(\mathbf{x})$ plot. (center) Valid positions according to (9), and (right) valid positions according to (9) and (10) with nnl1 = 0.01. (For interpretation of the references to color in this figure legend, the reader is referred to the web version of this article.)

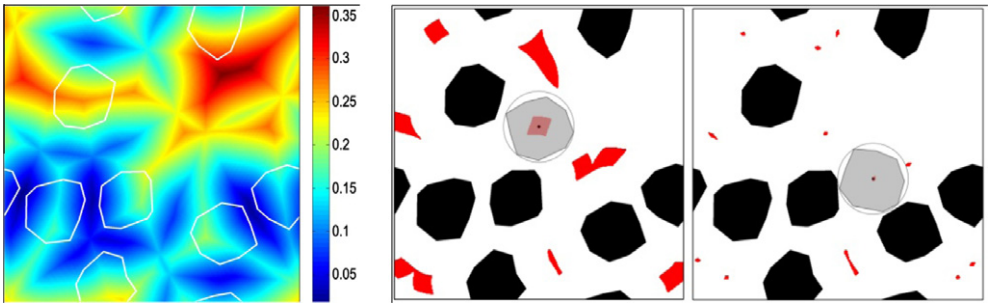

Fig. 9. Level set finder using LS_1 and LS_2. (left) $LS_2(\mathbf{x})$ plot. (center) Valid positions according to (9)–(11), with nnl1 = nnl2 = 0.06 (right) with nnl1 = nnl2 = 0.01.

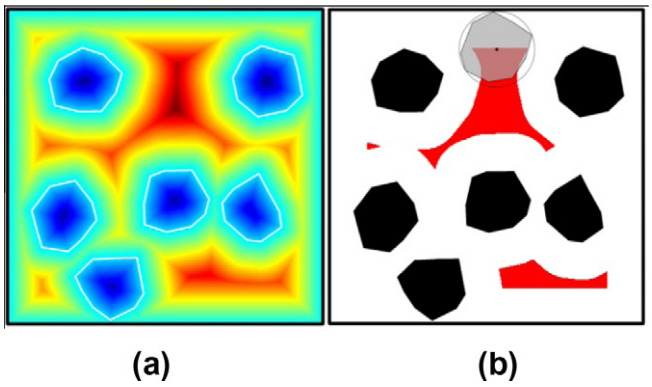

Fig. 10. Preventing inclusions from crossing RVE boundaries (a) $LS_1(\mathbf{x})$ with boundary contribution and (b) valid positions according to (9).

3.3. Performance evaluation of LS-RSA

Step 1: Linearity of the computation cost against the number of inclusions.

Each execution of the loop of a classical RSA computation basically takes the same time, irrespective of its success which depends on the current RVE density. Conversely, the LS-RSA algorithm which adds an inclusion at every loop thanks to the *finder* will take the same time to add any new inclusion irrespective of the current RVE density. In order to assess the performance excluding the influence of the adaptive refreshing, of the complex shape handle and of the nearest neighbors distance conditions, we first perform an addition of mono-sized circles with only the criterion for non-overlapping (9). Under such conditions, the time by loop is almost equal for classical RSA and LS-RSA and a simple comparison can be used to extract the exponential and linear trends of classical RSA and LS-RSA respectively. In other cases (i.e. arbitrary shaped inclusions), the time by loop may differ strongly due to important differences in the algorithms of both methods, and comparisons make less sense even if the trends are identical. Periodicity does not have an effect on the linear trend of LS-RSA cost, but takes substantially more time by inclusions. For circular inclusions this cannot be avoided but for complex shapes, the use of adaptive refreshing scheme will dramatically decrease the influence of periodicity (see Sections 2.3 and 2.4). Fig. 11 compares the computation cost for LS-RSA and classical RSA. Note that in this simplified case, the number of inclusions is linearly related to the density because all inclusions have the same size. All generations presented below are performed on a regular laptop, with RVE generation tools implemented in MatLab.

Step 2: Influence of nearest neighbor distances conditions.

Comparison with classical RSA in Fig. 12 shows that a substantial gain can be provided by the use of the *LS finder* complemented by nearest neighbor conditions (10) and (11) in terms of obtained density at no extra computational cost. This is in strong contrast with the Classical RSA methodology in which distance conditions increase dramatically the cost. Since the *LS finder* only uses cheap vector operations, the nature of the tested conditions has almost no influence on the global computation cost by inclusion while they allow improving the reached density of the packing.

Step 3: Influence of inclusions shape and benefit from the adaptive level set refreshing.

In case of arbitrary shaped inclusions (polygons or rounded polygons obtained by offset) the level set refreshing becomes the critical and costly operation. Its contribution in the global computation cost is linearly linked with the number of vertices defining the inclusions. The use of the adaptive refreshing scheme introduced in Section 2 brings its major advantage in this case. Fig. 13 compares the computational cost of LS-RSA with and without

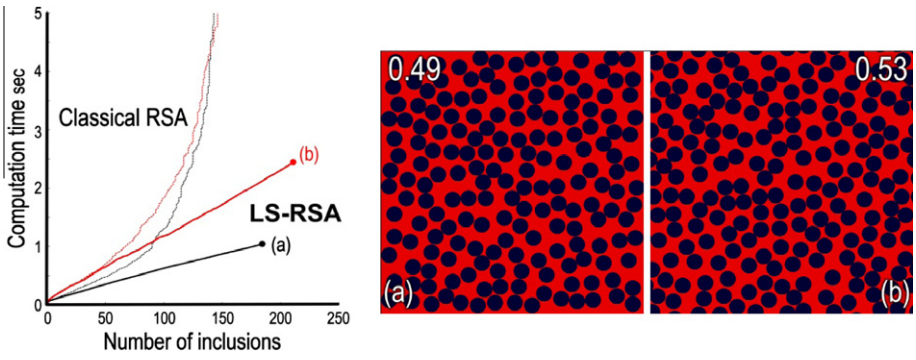

Fig. 11. Cost comparison between RSA and LS-RSA for non periodic (black curves) and periodic (red curves) RVEs. (The density reached is the number on each RVE figure). RSA curves are limited for readability but RSA produces the same RVE as (a) in 100 s and as (b) in 200 s. (For interpretation of the references to color in this figure legend, the reader is referred to the web version of this article.)

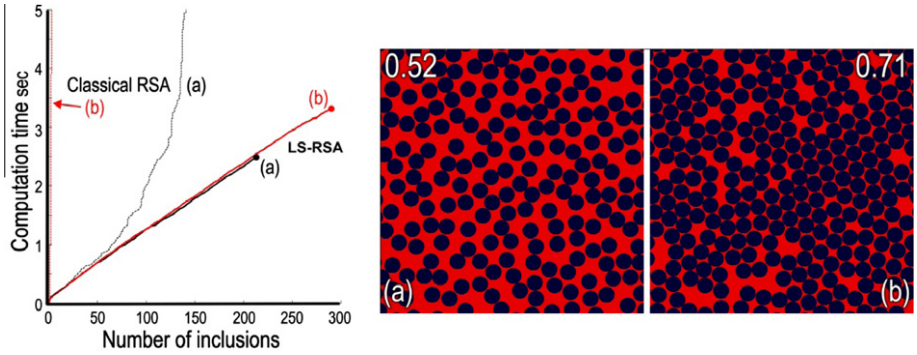

Fig. 12. Influence of nearest neighbor criteria (10) and (11). Full line correspond to the LS-RSA case. The dashed lines are equivalent generation with a classical RSA. (a) RVE generated with non-overlap criterion only (b) RVE obtained with conditions (9)–(11) with nnl1 = nnl2 = 0.005. The corresponding red curve for classical RSA shows that nearest neighbor control is not achievable without the *LS finder*. (For interpretation of the references to color in this figure legend, the reader is referred to the web version of this article.)

adaptive refreshing. Note that here the graph depicts the computation time as a function of the number of inclusions, which is not directly related to the density due to their arbitrary shape.

Step 4: Influence of inclusion shapes.

The main shape factor influencing density is not the number of vertices by inclusions but rather the ratio between the volume of inclusions and the volume of their SECs. This is due to the use of the SEC of inclusions to pilot the *LS finder* as illustrated in Fig. 8. Circular inclusions will therefore be packed at or near the theoretical maximal density [36,87], while quasi-regular polygons will leave more free space and elongated inclusions will lead to poor packing densities. Fig. 14 illustrates and quantifies this aspect.

Actually, any shape needing a particular rotation to be optimally placed among the existing ones will not perform optimally. This is the main limitation of the *LS finder* presented here. Solutions can however be implemented to avoid this inconvenience and will be discussed in Section 6. Classical RSA is less influenced by this effect as it uses the exact shape of inclusions to perform overlapping tests. Nevertheless, for elongated inclusion shapes, achieving dense packings requires the control of the inclusion orientations during the entire generation process. The classical RSA does not have possibility for this type of control and will also lead to poor packing for elongated inclusions due to the random orientation of inclusions.

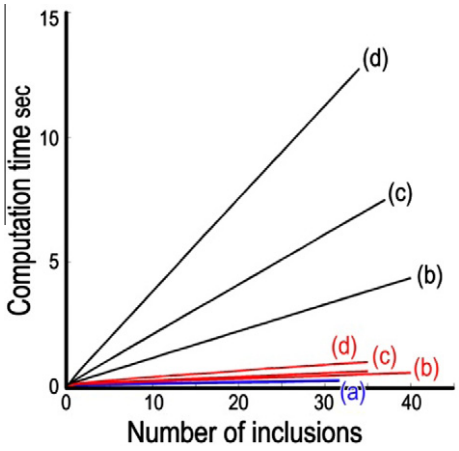

Fig. 13. Influence of adaptive level set refreshing rules on LS-RSA for (a) circular inclusions for which the adaptive refreshing does not apply, (b) 5-sided inclusions (c) 10-sided inclusions (d) 20-sided inclusions. Black curves are obtained without adaptive refreshing. Red curves use adaptive refreshing. (For interpretation of the references to color in this figure legend, the reader is referred to the web version of this article.)

Step 5: Effect of size distribution of inclusions.

It is obvious that an inclusion population with a significantly distributed size distribution will allow reaching higher densities more easily. Fig. 15 illustrates this for a population with grains size varying with a factor of about 50 as it can be encountered in soils.

These (periodic) RVEs are typically generated in about 15 s for (**b**) and 35 s for (**a**) on a regular laptop under MatLab. Using a classical RSA implementation without *LS finder*, this type of generation can quickly become unaffordable, because the addition time by inclusion is exponentially increasing with density as explained and because the number of inclusions needed to increase density of a constant density increment is also increasing, due to the decreases of inclusion size.

For mono-sized inclusions the computation time is linear with the number of added inclusions and with the density. For multi-sized populations, the linearity of the cost against the number of inclusion is kept but not against the density because the latter increases more slowly with small inclusions than with large ones. To illustrate this we consider a uniform distribution for the inclusion size. This means that each size interval will represent about the same volume fraction in the RVE. Largest inclusions will therefore represent a small number compared to the number of small inclusions (see Table 1).

With adaptive level set refreshing, the time by inclusion (in addition to be 60 times faster than without) decreases with the size of inclusions since the influence zone for LS refreshing becomes smaller and the level set refreshing time dramatically decreases. Large inclusions are generated first. The computation cost then quickly decreases with the number of generated inclusions. In terms of time by increment of density (δd), this mechanism thus counterbalances the increase of the number of inclusions by δd and restores the linearity of the computation cost against the density until a given inclusion size. After this critical size, the level set evaluation time becomes negligible in the loop and the optimal time by inclusion (about 100 inclusions/s) is reached and kept constant, which results in an increase of the time for a given δd, see Fig. 16.

4. Level set based tools for complex microstructure generation

4.1. Inclusion morphing for densification and shape modification

The density that can be reached with a RSA algorithm, even enhanced with a level set control is limited to finite values depending on the inclusion shapes and the size distribution as discussed before. The spatial organization cannot depend on the inclusion shapes, this is a limitation to produce very close packings in which

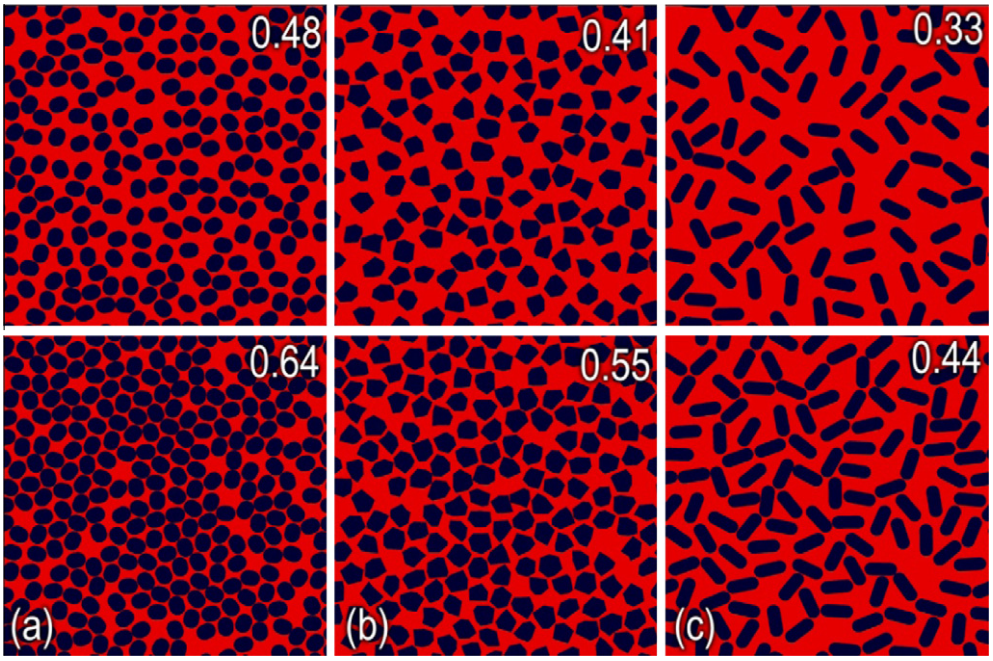

Fig. 14. Influence of inclusion shapes on maximum density achievable by LS-RSA. (Top) generations with non-overlap criterion only, (bottom) generation with conditions (9)–(11) with nnl1 = nnl2 = 0.005. (a) Slightly elongated inclusions, (b) 7-sided random polygons and (c) elongated inclusions.

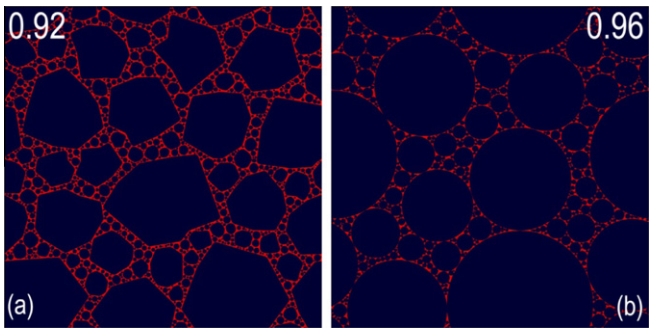

Fig. 15. Multi-sized population RVE generation with (a) 1089 arbitrary shaped inclusions and (b) 566 circular inclusions. Those RVEs were produced with a double precision grid for level set functions evaluations.

Table 1
Size distribution of inclusions resulting from generation of Fig. 16.

Size (radius) interval	0.205/0.155	0.155/0.105	0.105/0.055	0.055/0.005
Volume fraction	0.210	0.197	0.203	0.199
Inclusion number	3	6	18	217
Shape	Quasi-regular 5-sided random polygons			

the position and orientation of inclusions match the surrounding inclusions shape as it could be observed in real packing of sand or rock assemblies.

The level set formalism allows modifying the inclusion shapes by morphing and densifying the RVEs with respect to the spatial organization. At the limit, it leads to RVEs of density equal to 1 with completely side-by-side inclusions and may therefore be used to generate polycrystal-like microstructures.

This may be achieved using the following concept. If the iso-zero curve of $LS_{\Phi 1}(\mathbf{x})$ and $LS_{\Phi 2}(\mathbf{x})$ defines the interfaces of two inclusions Φ_1 and Φ_2, then the iso-zero level of $|LS_{\Phi 1}(\mathbf{x}) - LS_{\Phi 2}(\mathbf{x})|$ defines the locus of equal distances between these two inclusions, see Fig. 17. This curve divides the domain in two sub-domains, one for each inclusion gathering all the points closer to this inclusion than to the other one. The absolute value is important to attribute the same sign to both sub-domains. Any isocontour of this function will therefore define one curve for each inclusion.

For the case of two inclusions, this operation is equivalent to $LS_2(\mathbf{x}) - LS_1(\mathbf{x})$ because for any $\mathbf{x}$ satisfying $LS_{\Phi 1}(\mathbf{x}) > LS_{\Phi 2}(\mathbf{x})$, $LS_2 = LS_{\Phi 1}(\mathbf{x})$ (inversely if $LS_{\Phi 1}(\mathbf{x}) < LS_{\Phi 2}(\mathbf{x})$), and hence the absolute value is dropped while writing the statement in terms of LS_1 and LS_2.

For multiple inclusions, the iso-zero curve of $LS_2(\mathbf{x}) - LS_1(\mathbf{x})$ defines a diagram in the RVE in which each cell encloses an inclusion and defines the locus of points closer to this inclusion than to the other ones, see Fig. 18, exactly as the Voronoï diagram acts for point distributions.

Many intermediate situations can be found between the undistorted (initial) inclusions and Voronoï-like cells produced by $(LS_2(\mathbf{x}) - LS_1(\mathbf{x}))$. Such configurations can be obtained by replacing original curves Φ_i of inclusions boundaries by extracting new curves Φ_{new} from the iso-zero curve of the function $O_l(\mathbf{x})$ defined as

$$O_l(\mathbf{x}) = LS_1(\mathbf{x}) - LS_2(\mathbf{x})\gamma + t. \tag{12}$$

With $\gamma = 1$, this function increases the size of inclusions until a joint of constant thickness t is obtained between inclusions. The coefficient γ allows (quite qualitatively) to give more or less importance to the shape of the transformed inclusions. In relation (12) LS_1 and LS_2 have been inverted to attribute the negative sign to the inclusion domain, as before. Results for different values of γ in Table 2 are depicted in Fig. 19.

The prescribed distance t cannot be less than the precision h of the discretisation grid for LS_1 and LS_2, as for smaller values, inclusions collapse as already discussed in Section 2.3. However, the offset technique presented in previous Section 2.5 can be used a posteriori on inclusions with an offset distance d relative to the t parameter used in (12) to reduce or eliminate (if $t = 2d$ and $\gamma = 1$) the inclusion inter-distance as depicted in Fig. 20(b), generating particles in contact, as can be met for instance in concrete.

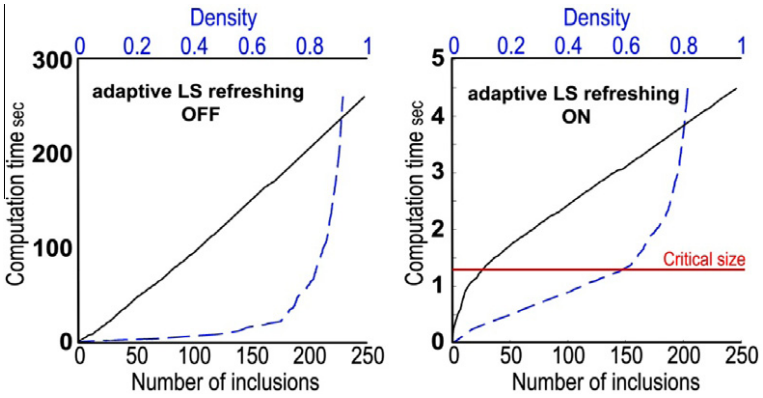

Fig. 16. Generation of multi-sized inclusions, comparison between the time against the number of inclusions (continuous) and the time against the density (dashed) with and without adaptive refreshing.

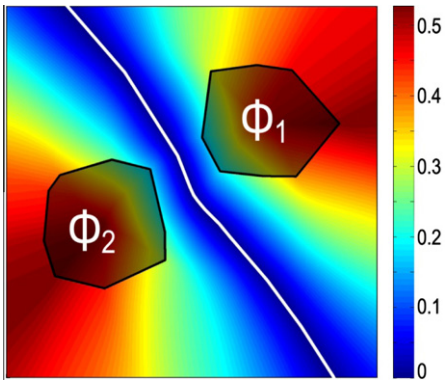

Fig. 17. $|LS_{\Phi 1}(\mathbf{x}) - LS_{\Phi 2}(\mathbf{x})|$ and the iso-distance locus.

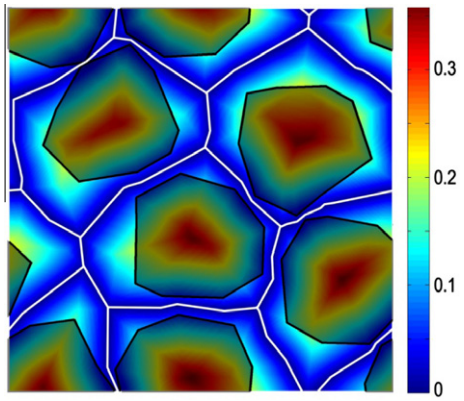

Fig. 18. $LS_2(\mathbf{x}) - LS_1(\mathbf{x})$ and the iso-distance curve (white lines) delimiting Voronoï-like cells.

Table 2
Parameters for RVE in Fig. 19.

RVE	(a)	(b)	(c)	(d)	(e)	(f)
t	/	0.005	0.005	0.005	0.005	0.035
γ	/	0.2	0.5	0.8	1	1.5

Furthermore, it may be convenient in specific cases to perform this morphing and inclusions growth only on a selected part **A** of the starting inclusion population in the RVE, leaving the other ones **B** unchanged. This requires evaluating LS_1 and LS_2 independently for both population. This opens a large range of possibilities. A simple illustration of complete expansion of the inclusions **A** with no modification of inclusions **B** is given now. A function achieving this can be constructed starting from $LS_{\mathbf{A}2}(\mathbf{x})$-$LS_{\mathbf{A}1}(\mathbf{x})$. Values of this function have to be modified in domains inside the **B** inclusions and for any point **x** lying closer to a **B** inclusion than to a iso-distance curve of population **A**. This latter distance is measured by $(LS_{\mathbf{A}2}(\mathbf{x}) - LS_{\mathbf{A}1}(\mathbf{x}))/2$. The final function $O_{II}(\mathbf{x})$ to use can therefore be constructed as follows and is illustrated in Fig. 21.

$$O_{II}(\mathbf{x}) = -|\min[(LS_{A2}(\mathbf{x}) - LS_{A1}(\mathbf{x}))/2, LS_{B1}(\mathbf{x})]|. \quad (13)$$

4.2. Bridging and coating phase generation

A large part of the microstructures observed in real materials are more than just an assembly of particles within a single matrix. Usually RVEs need additional features to properly mimic the intrinsic fabric of such materials. Fig. 22 illustrates two typical examples for which a third phase has to be taken into account for microstructural modeling. The first consists of bridges present in clayey soils due to clay minerals agglomeration between larger grains of hard minerals, while the second is the interfacial transition zone between particles and the cement paste of concrete due to specific hydration conditions near the hard surfaces of particles. Similarly, in partially water saturated granular materials (e.g. soils), capillary meniscus are a particular form of bridging phase that links particles together [17].

Generating such additional phases in RVEs cannot be performed easily by a classical inclusion addition/packing approach. Furthermore, these features are "semi-random" because they have to be "grown" respecting specific microstructural "rules", starting from an existing random inclusions distribution.

The presented level set tools can be combined to generate RVEs containing a third phase bridging or coating inclusions. Until now, the RVE domain Ω was split in two sub-domains, Ω_i for the existing inclusions and Ω_m for the remaining continuous medium. The purpose now is to separate Ω_m in two sub-domains: Ω_f for a third phase grown from the inclusions and denoted here as the "fabric" sub-domain, and Ω_r for the remaining medium, see Fig. 23. Here again, the iso-zero curve of a function $O(LS_1(\mathbf{x}), LS_2(\mathbf{x}), \ldots)$ will be used for the extraction of the boundary curves between Ω_f and Ω_r, depending on the starting inclusion distribution, and with respect to some governing parameters.

Note that terms "inclusions" and "matrix" will keep the same meaning as before, having a more geometrical connotation. The word "inclusions" will still be used for any feature defined by a closed curve and "matrix" will still be used to denote the remaining

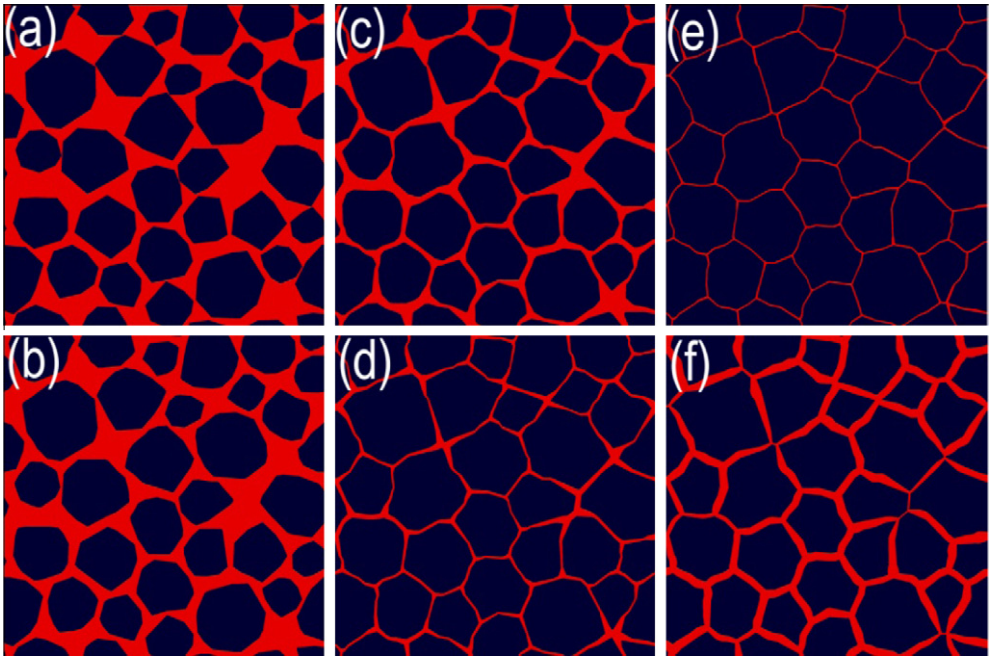

Fig. 19. Result of partial morphing of inclusions with function (12). All RVEs are obtained with the same set of initial inclusions (a).

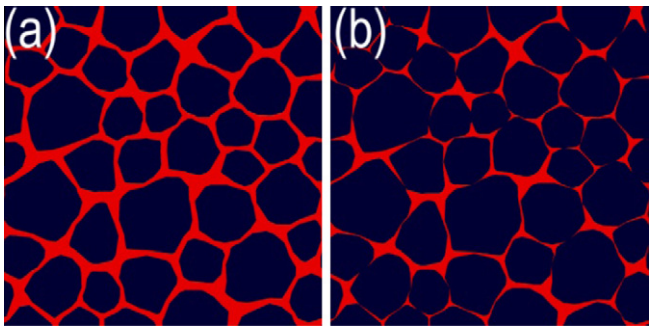

Fig. 20. Vanishing the minimum inclusion inter-distance with an offset. (a) Original RVE obtained from a particle distribution morphed using function (12), $t = 0.006$ and $\gamma = 0.5$. (b) Resulting RVE with an offset of 0.0055.

domain, i.e. the RVE domain except all inclusion sub-domains. For example, in Fig. 23 Ω_r and Ω_i will be considered as inclusions in the matrix Ω_f.

Using the level set formalism, various combination allow producing coating and bridging between particles of a given distribution. The simplest case of uniform coating of particles can be achieved by extracting the curves defined by the function

$$O_{III}(\mathbf{x}) = \mathrm{LS}_1(\mathbf{x}) - w = 0, \tag{14}$$

where w is the thickness of the coating. This thickness can be made dependent on inter-particles distances using the following function

$$O_{IV}(\mathbf{x}) = \mathrm{LS}_1(\mathbf{x}) \cdot \mathrm{LS}_2(\mathbf{x})^{\kappa} - w, \tag{15}$$

in which the exponent κ can be used to obtain different results such as bridges (positive values) or cracks (negative values). Examples of the effect of κ given in Table 3 on RVE generation are illustrated in Fig. 24.

The study of a particular material microstructure requires generating RVEs while controlling explicitly some measurable features. Such features depend on parameters which differ from the introduced κ and w and the function $O_{IV}(\mathbf{x})$ may have to be written in an alternative way to make the use of the required parameters possible. The following Section 4.3 presents an example of such a development for the quantitative control of bridges volume fraction or length. Similar manipulations could be used for other specific microstructural features (i.e. initial micro-cracking, non-uniform coating, patterned porosity, ...) but fall out of the scope of the present contribution.

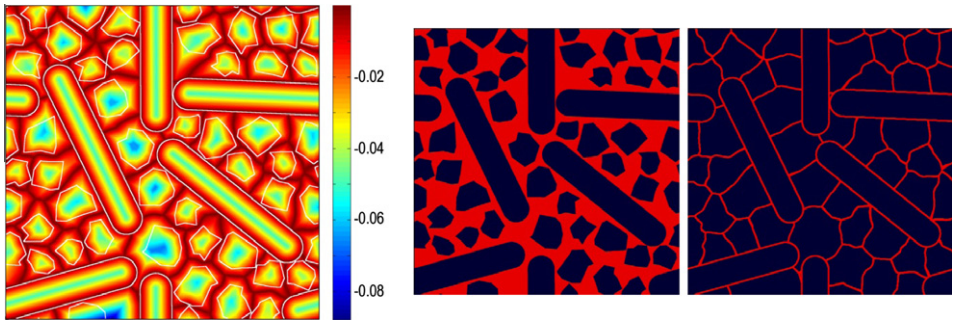

Fig. 21. Selective morphing of inclusions with elongated inclusions kept fixed (population B), while the size of others is increased. (left) Plot of the function defined by (13), (center) original microstructure and (right) resulting microstructure.

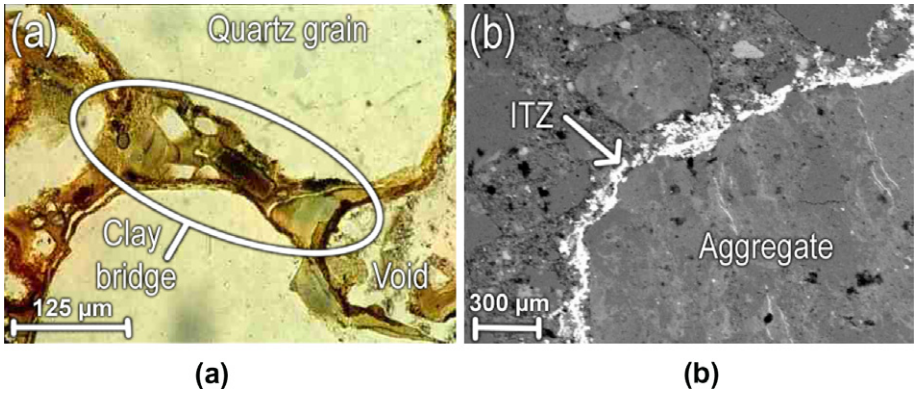

Fig. 22. Examples of microstructural fabric requiring the incorporation of a third phase. (a) [9] Clay bridge in a soil made of quartz (sand) and clay minerals. (b) [68] Interfacial transition zone around a large particle in concrete (artificially colored for visualization).

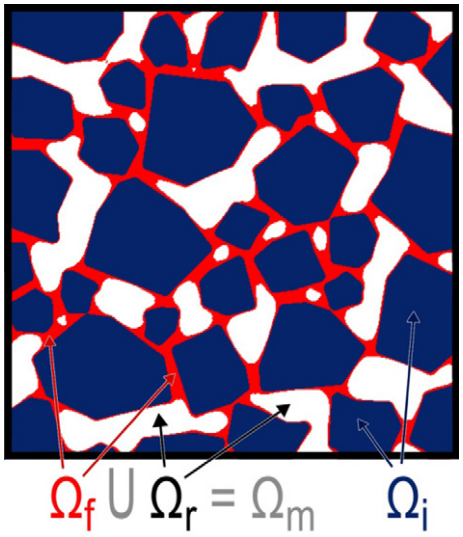

Fig. 23. Definition of the fabric domain Ω_f (red) and the remaining domain Ω_r (white) which subdivide the original Ω_m domain. (For interpretation of the references to color in this figure legend, the reader is referred to the web version of this article.)

Table 3
Parameters for RVE in Fig. 24.

RVE	(a)	(b)	(c)	(d)	(e)	(f)
w	0.01	0.02	0.0001	0.0003	2	35
κ	0	0	1	1	−1.5	−2

4.3. Quantitative control of coating and bridges

The function defined in (15) with a positive exponent κ may directly be used to produce bridging but does not offer a strong quantitative control on microstructural features (e.g. fabric volume fraction, length of bridges, ratio bridges/fabric, etc. are not explicitly controlled). For this purpose, one can use the function $LS_1(\mathbf{x}) + LS_2(\mathbf{x})$ which contains more directly the distance between two close inclusions. Explicitly, for every $\mathbf{x}$ in Ω, $LS_1(\mathbf{x}) + LS_2(\mathbf{x})$ is the length of the shortest path to link the two nearest inclusions via $\mathbf{x}$, as illustrated in Fig. 25a. This function therefore appears to be appropriate to construct bridges with a proper control on their length.

To generate bridges from this, one could use the function

$$O_V(\mathbf{x}) = LS_1(\mathbf{x}) + LS_2(\mathbf{x}) - b, \tag{16}$$

where b would be the prescribed length of the bridges. However, unlike the previously introduced functions, Eq. (16) does not produce iso-zero level curves entirely included in Ω_m. As a result, it must be combined with $LS_1(\mathbf{x})$ in a minimization to ensure that the Ω_r domain does not overlap with the Ω_i domain, as illustrated in Fig. 25b.

Using an additional parameter in the function allows controlling both the coating thickness and the bridges length with the same statement as follows:

$$O_{VI}(\mathbf{x}) = \min[LS_1(\mathbf{x}) + LS_2(\mathbf{x}) - b, LS_1(\mathbf{x}) - w], \tag{17}$$

where w is the coating thickness and b the bridges length. Such parameters can be used directly in the function or can be deduced from prescribed volume fractions obtained through experiments. The volume fraction of the fabric will be denoted here $\underline{\lambda}_1$ and the bridging material is assumed to represent a volume fraction $\underline{\lambda}_2$ of the fabric material.

The volume of the different sub-domains of Ω_{RVE} should therefore satisfy the following relations. The volume of inclusions is fixed by

$$V_i = \int_\Omega (LS_1(\mathbf{x}) < 0) d\Omega. \tag{18}$$

The coating volume depends on w only and is given by

$$V_c(w) = \int_\Omega (LS_1(\mathbf{x}) - w < 0) d\Omega - V_i, \tag{19}$$

where V_i is evaluated by (18), while the bridges volume depends on both w and b according to

$$V_b(w,b) = \int_\Omega (O_{VI}(\mathbf{x}, w, b) < 0) d\Omega - V_c(w) - V_i. \tag{20}$$

With the imposition of $\underline{\lambda}_1$ and $\underline{\lambda}_2$ and assuming as before a unit size RVE, the following constraints need to be imposed on the generation process

$$V_c(w) + V_b(w,b) = \underline{\lambda}_1, \tag{21}$$

$$V_c(w) = \underline{\lambda}_1 \cdot (1 - \underline{\lambda}_2). \tag{22}$$

These two equations are non-linear (due to the non-linearity of the integrand in V_c and V_b expressions against b and w), and are easily solved for w and b, separately if (22) is solved first, with a simple iterative procedure. Computationally, LS_1 and LS_2 are evaluated for a regular discrete set of N points $\mathbf{x}_n$ with $n \in \{1{:}N\}$ and relations (18)–(20) become simple and fast vector operations. For instance, (19) becomes

$$V_c = N^{-1} \sum_n [(LS_1(\mathbf{x}_n) - w) < 0] - V_i. \tag{23}$$

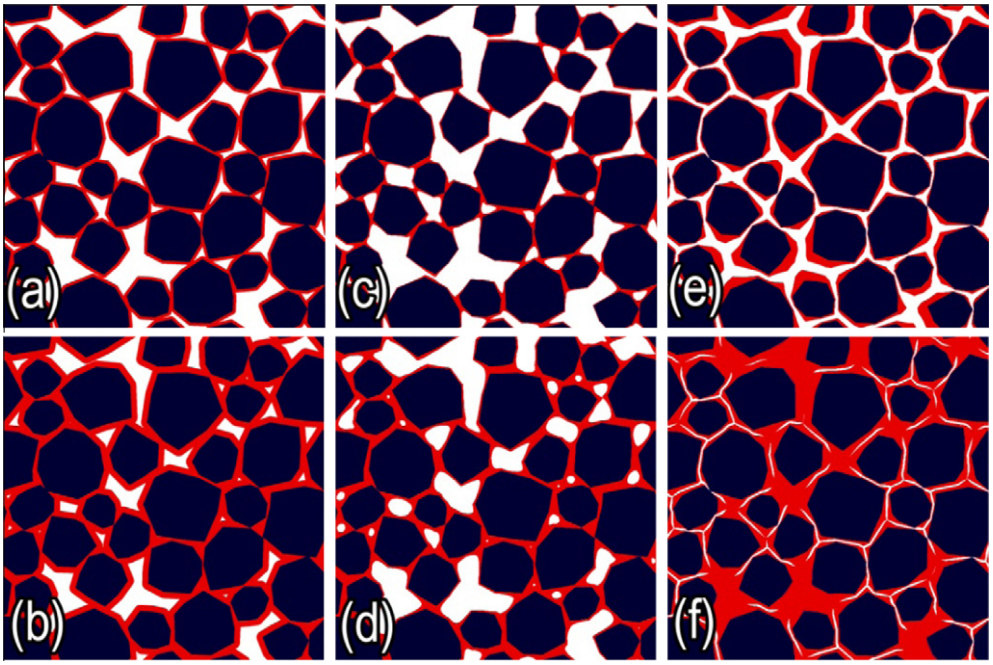

Fig. 24. Fabric formation using the operating function (15) for different values of parameters w and κ.

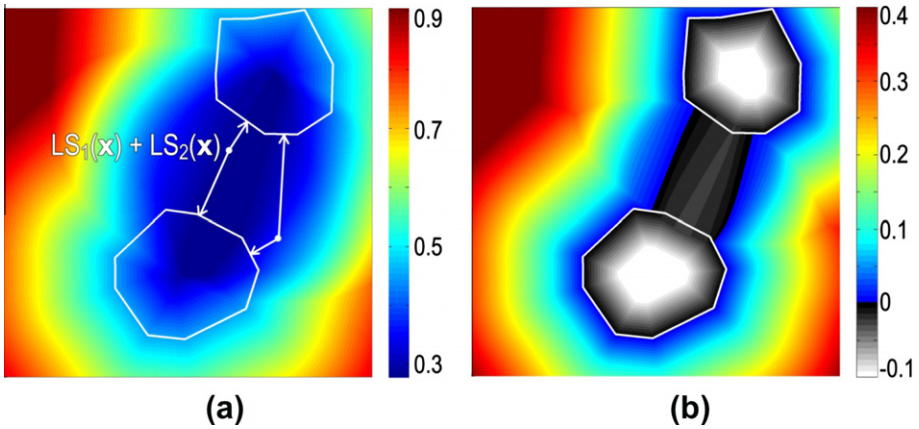

Fig. 25. (a) $LS_1(\mathbf{x}) + LS_2(\mathbf{x})$ and geometrical interpretation, (b) $\min[LS_1(\mathbf{x}) + LS_2(\mathbf{x}) - b, LS_1(\mathbf{x})]$, ($b = 0.3$). The colored area is the remaining media domain Ω_r. White lines enclose the Ω_i domain, the fabric domain is then only the bridge.

These relations are used in two loops for (22) first and then (21) in order to evaluates λ_1^* and λ_2^* for trial values w^* and b^* until the convergence to $\underline{\lambda}_1$ and $\underline{\lambda}_2$ is observed. Based on examples treated below and in the application section, even the most complex RVEs do not require more than 5–10 steps to converge. The addition of this procedure is thus of no major influence on the computation time. The main costly operation is again to evaluate LS_Φ for the newly extracted curves. However, this evaluation can be avoided here if the RVE generation is complete with the added features and if no level set is needed for post generation purposes (e.g. if only discrete definitions of curves are needed for a finite element mesh construction). Fig. 26 shows different RVEs generated with different values of $\underline{\lambda}_1$ and $\underline{\lambda}_2$ reported in Table 4.

5. Applications

5.1. Clay/sand mixed soils

As a first application of the proposed framework for real materials, a silty soil (Marche-les-Dames soil, denoted as MLD) is considered, based on its experimentally determined size distribution function given in Fig. 27 [16]. Such a soil is made of inert particles (sand and silt), clay bridges as well as voids.

The following RVE generation methodology is used, considering that the matrix material actually consists of the bridging and surrounding clay, and that the inclusions are the voids and the inert sand particles. It is assumed that distances are scaled to be expressed in units relative to the RVE size (i.e. in developments, phase volumes are equal to volume fractions and the RVE volume is equal to 1).

The particles are first generated with LS-RSA, enforcing inclusions inter-distances to be proportional to the particles size thereby obtaining an homogeneous distribution, leaving enough free space for voids addition. Based on the measured size distribution, minimal and maximal particles sizes of 2 and 80 μm are considered. All the solid material lower than 2 μm in size is considered as clay. Since the experimental size distribution function only relates to the solid phase (without voids), a volume fraction of the voids V_{void} has to be assumed and used to derive the real volume fraction of particles by multiplying those given in Fig. 27 by $(1 - V_{\text{void}})$.

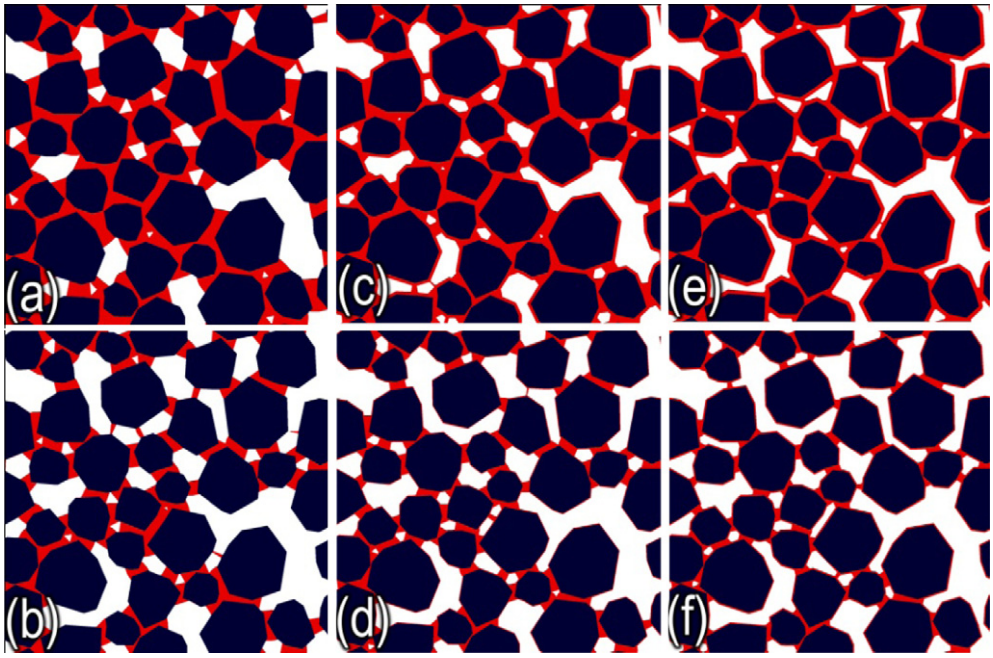

Fig. 26. Bridge and coating for various volume fractions and a bridge/fabric ratios reported in Table 4.

Table 4
Parameters for RVE in Fig. 26.

RVE	(a)	(b)	(c)	(d)	(e)	(f)
$\underline{\lambda}_1$	0.15	0.05	0.15	0.05	0.15	0.05
$\underline{\lambda}_2$	1	1	0.75	0.75	0.5	0.5

The resulting matrix is then divided in a fraction of void and clay bridges with the procedure described in Section 4.3. The void ratio V_{void} and the clay fraction V_{clay} are used to derive the $\underline{\lambda}_1$ parameter with $\underline{\lambda}_1 = (1 - V_{\text{void}}) \cdot V_{\text{clay}}$. Parameter $\underline{\lambda}_2$ will be chosen to 0.8 based on qualitative observations since no quantitative experimental measurement are available for this parameter. The voids volume fraction will here be chosen as 10% and 15% for 2D RVE generations. Note that practically a higher void volume fraction would be met in real 3D experimental specimens. The volume fraction of solid phase below 2 μm V_c is measured to be 16% from the size distribution.

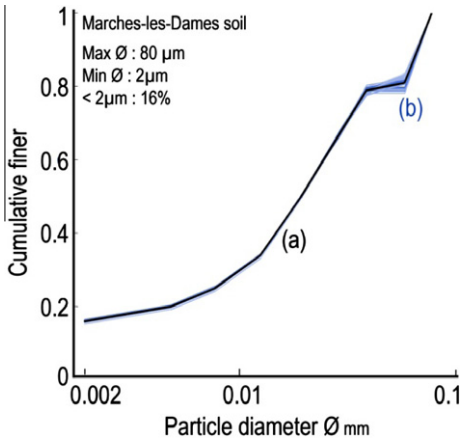

Fig. 27. Particles size distribution for the MLD soil. The 0.16 fraction not shown in the graph are the clay minerals, assumed to be a continuous medium. (a) Black curve, measured on a real specimen used for inputs [16]. (b) Blue curves, distributions of 45 generated RVEs of size 0.48 mm × 0.48 mm. Examples of such RVEs are depicted in Fig. 28. (For interpretation of the references to color in this figure legend, the reader is referred to the web version of this article.)

Based on this data, the microstructural RVEs depicted in Fig. 28 have been generated. Note that these are only a few of the RVEs which could be generated since the generation time is rather short, on the order of 10 s on a regular laptop. Approximately 30% of this time is required to generate level set for void inclusions needed for a subsequent X-FEM computation on the RVE. For explicit FEM discretisation, as explained in Section 4.3, the generation time can be reduced to around 6–7 s.

As can be seen from Fig. 27, all the generated RVE present a particle size distribution in very good agreement with the input experimental distributions.

It should be mentioned that in real specimen of such a soil, the measured fraction of void is composed of macro-voids between large particles, as those generated here and also micro-voids at the clay minerals scale that should be added in the clay fraction to have a complete representation of the material. In the generated RVE presented here, only the macro-voids have been taken into account for simplicity, this is another reason why the real void volume fraction is higher in real specimens. If the micro/macro-void ratio is known (e.g. by mercury absorption measurements), it could straightforwardly be used in the presented generation process, considering the clay/micro-void mix as a continuous medium. In a multi-scale physical modeling context, this is a consistent approach since it is cumbersome to determine experimentally the needed properties (mechanical or other) of isolated clay without any void (and it probably would not make any sense).

5.2. Bimodal polycrystalline microstructures

A large number of recent works in the literature is devoted to the study of the mechanical properties of single phase or multiphase polycrystalline aggregates, see [64,6,1,81,54,61,43,62] for a non-exhaustive list of contributions. Various mechanical models are used for such studies such as crystal plasticity formulations or size dependent (gradient) plasticity. A significant portion of these papers makes use of computational studies to investigate the macroscopic effects of microstructural properties. A commonly

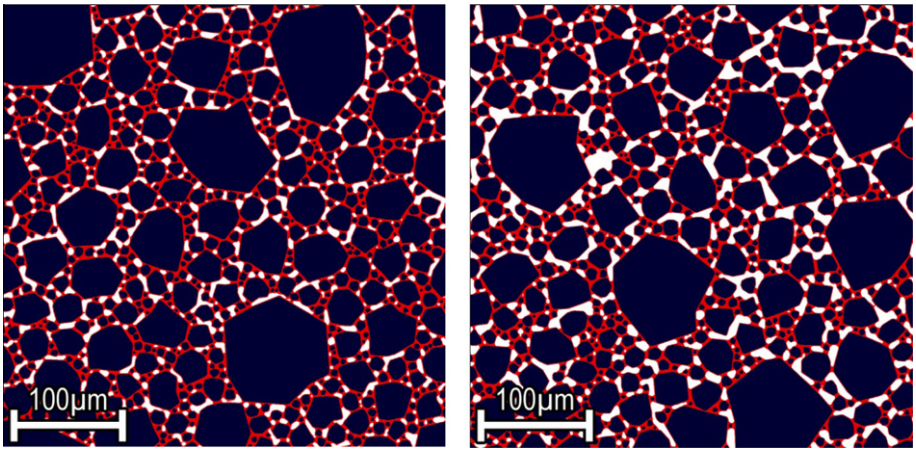

Fig. 28. Example of soil RVEs generated with a void fraction of (left) 10% and (right) 15%. Dark blue: inert grains, red: clay matrix, white: voids. Those RVEs were produced with a double precision grid for level set functions evaluations. (For interpretation of the references to color in this figure legend, the reader is referred to the web version of this article.)

faced issue by such contributions is the generation of RVEs which have to be used in computational homogenization. Various strategies have been used to generate such polycrystalline microstructures, among which the Voronoï tessellation based methods was one of the most effective.

Size effects in polycrystals have been a topic of intensive computational investigations over the last decade based on size-dependent models to describe the yield stress increase as well as the decrease of ductility with grain size refinement in the submicronic range [3,43]. Experimental efforts now focus on processing routes which allow increasing yield stresses while restoring ductility. One of the routes to reach this objective is to produce metals with bimodal grain size distribution, i.e. containing large grains embedded in a continuous phase of submicronic grains [89]. Such an improvement can be reproduced qualitatively using size dependent plasticity models as shown in [43] on a single RVE computation. However, the generation of polycrystalline aggregates with controlled bimodal grain size distribution is a complex task, and such computations should theoretically be reproduced for several randomly generated RVEs.

For the sake of illustration, the morphing strategy presented in Section 4 will now be applied to such a RVE generation. Focusing on the experimental example given in [89], a RVE for bimodal polycrystalline microstructure will be generated here. The grain size distribution is essentially bimodal, with a population of large grains with a size around 1700 nm in a continuous phase of fine grains with a size around 190 nm. The large grains represent around 25% of the volume fraction. The methodology presented in Section 4.1 is used to produce the polycrystalline pattern. In order to precisely control the size and volume fraction of grains, a specific procedure is followed.

The larger grains are generated first by LS-RSA giving them directly their final shape, size and volume fraction. This generation is governed without distance criterion in order to have a completely random distribution and enforcing periodicity. Then the distribution of small grains is obtained again with LS-RSA inclusion addition but giving them a size which depends on average inter-inclusion distances. This distance is finally decreased by selective morphing as explained in Section 4.1 on the latter population in order to keep volume fraction, size and shape of large grains unchanged. This operation fills all the remaining space with small grains. If the initial inter-inclusion distances (explicitly controlled by the *LS finder*) were properly deduced to the targeted size for small grains at the sequential addition step of the second population, an exact experimental size distribution could be respected. The shape of grain boundaries depends strongly on the inclusion shape before the selective morphing step and can thus also be controlled as circular inclusions generate almost straight boundaries, while irregular polygons lead to distorted boundaries.

Fig. 29 depicts RVEs generated for two different variabilities on size distribution of the small grains population. This variability can actually be trivially controlled at the LS-RSA stage since the *LS finder* can easily perform a uniform inter-inclusion distance distribution, the selective morphing then adds the same constant to each inclusion size.

5.3. Natural rocks masonry

As a third example, RVEs for irregular masonry are now generated. The mechanical behavior of masonry has been investigated through computational homogenization techniques in several publications, both at the material level [48,44] and at the structural scale [45]. Most of the available contributions however relate to the case of periodic masonry in which constituents are stacked in a regular fashion. Recently a number of contributions tackled the problem of homogenization for irregular stone masonry, for which the size of the RVE becomes a crucial issue [49,50]. Other works were related to methodologies allowing the identification of statistically equivalent periodic unit cells for such disordered materials [94,69,37].

The generation of random disordered microstructural RVEs for such a material is therefore of prime importance. The presented level set based tools can efficiently be used for a fast generation of such RVEs for natural rock masonry. First, elongated and oriented inclusions are generated with LS-RSA in order to define a basis for the random alignment of blocks. Then, the function defined by relation (12) is used in order to obtain a quasi constant thickness joint between blocks. RVEs generated with this procedure are represented in Fig. 30.

The generation of such RVEs is almost computationally free (generation time lower than 5 s), and can be used to generate a large range of patterns by modifying the starting distribution or the used function. In addition, a specialized *LS finder* can be formulated to offer more possibilities for specific block organizations. Moreover, if observations suggest it, a fraction of existing open cracks in mortar joints can easily be added using the function illustrated in Fig. 24f.

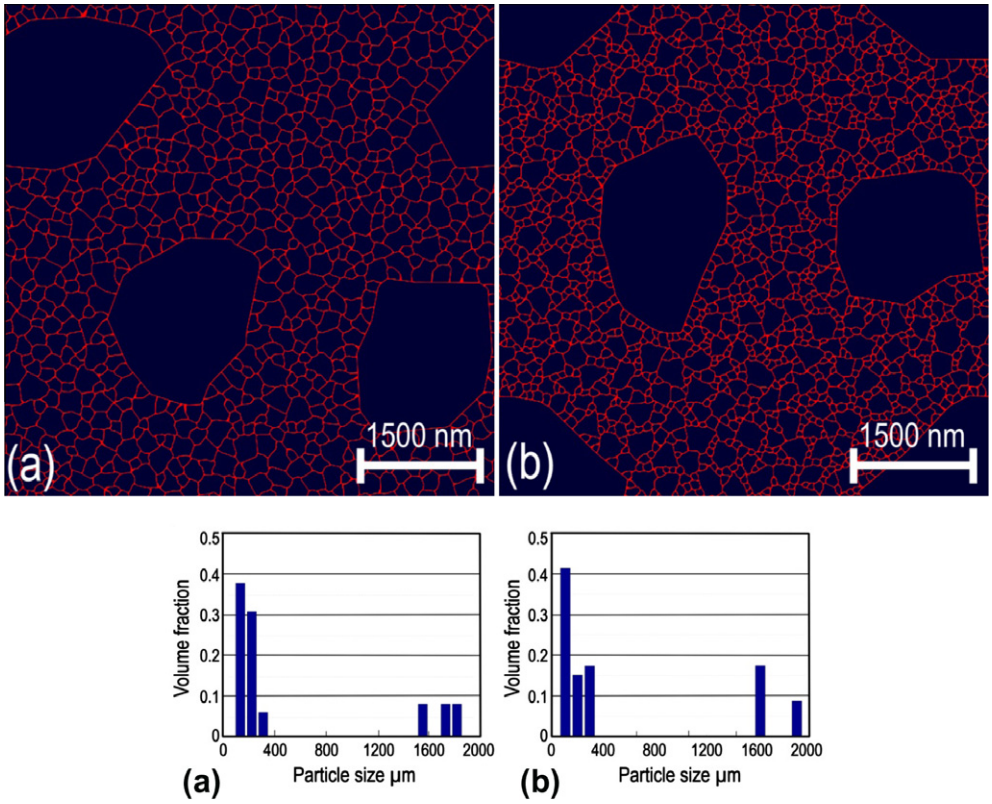

Fig. 29. Example of bimodal polycrystalline RVE generated, fraction of large grains: (a) 24.8% and (b) 26.1%. Those RVEs were produced with a double precision grid for level set functions evaluations.

6. Discussion

A number of points can be discussed concerning the proposed RVE generation framework.

First, it is emphasized that all the presented tools may easily be extended for 3D RVE generation. The level set concepts are indeed already well developed and used for 3D modeling issues as performed in [51,85]. The computational cost will of course inevitably increase for the case of 3D microstructures. However, the benefit with respect to a pure RSA based generation could be even more important [25]. Furthermore, other level set based operations presented in Section 4 may be used to implicitly handle complex and intricate situations in 3D RVEs which can become cumbersome when considering explicit surfaces definitions for operations such as bridging and/or coating formation.

Second, the level set enhanced RVE generation may be viewed as an ideal pre-processing tool for level set XFEM discretisation techniques and FFT-based homogenization algorithms. XFEM methodologies are now available for taking into account implicitly material boundaries independently from the mesh as proposed in [80,51,18,23,24,85]. The level set functions required in those methods are indeed a by-product of the present generation tool. FFT-based homogenization methods are also available to evaluate overall properties of heterogeneous materials using images of their microstructures as the main input of the model [52,53,46]. Such images are used to attribute material properties to voxels and equations of the homogenization problem are solved in a Fourier space obtained by FFT of a specific stress field (which is a function of the image used as material map). The RVE generation methodology proposed in the paper can indeed be directly adapted to produce maps of material properties instead of discretization of interfaces (needed for FEM meshes) or level set functions of interfaces (needed for XFEM). As another potential benefit, efforts have been made to develop tools for meshing implicit geometries defined by level set functions as presented in [58]. This technique may be a natural way to generate fast and very accurate meshes from the level set functions implicitly defining the generated RVE features.

It should be mentioned that a current limitation of the framework is, *at the LS-RSA stage*, related to the definition of an equivalent inclusion size based on the SEC of the inclusion shape when selecting potential positions to place it in the RVE. This choice implies that a population consisting of mainly elongated inclusions would lead to poor packing densities as the largest dimension of such an inclusion would be used to identify its potential position in the RVE. This drawbacks actually holds for any shape needing a particular rotation to be optimally placed beside the existing inclusions. The same drawback is present if highly non convex inclusion imbrications need to be considered. Three potential remedies could be investigated to adapt the proposed tools to this type of inclusions:

- *Classical methods*. Any classical method of the DEM family can be used to end the generation process.
- *Purely level set methods*. An "orientation sensitive LS finder" could be formulated using potentially three principles. The first may use the quantity $\partial LS_1(\mathbf{x})/\partial \mathbf{x}$ to know the *direction* in which the nearest inclusion from $\mathbf{x}$ is to be found. This information could then be used to give a particular orientation to the new inclusion with the best match with existing inclusions position. The second possibility uses straight segments of iso-w curves of $LS_1(\mathbf{x})$ to directly choose elongated free space of width w. Finally a third possibility applying only for globally oriented or distorted RVEs. Any transformation of coordinates can be used between the level set space and the RVE space, and the inclusion

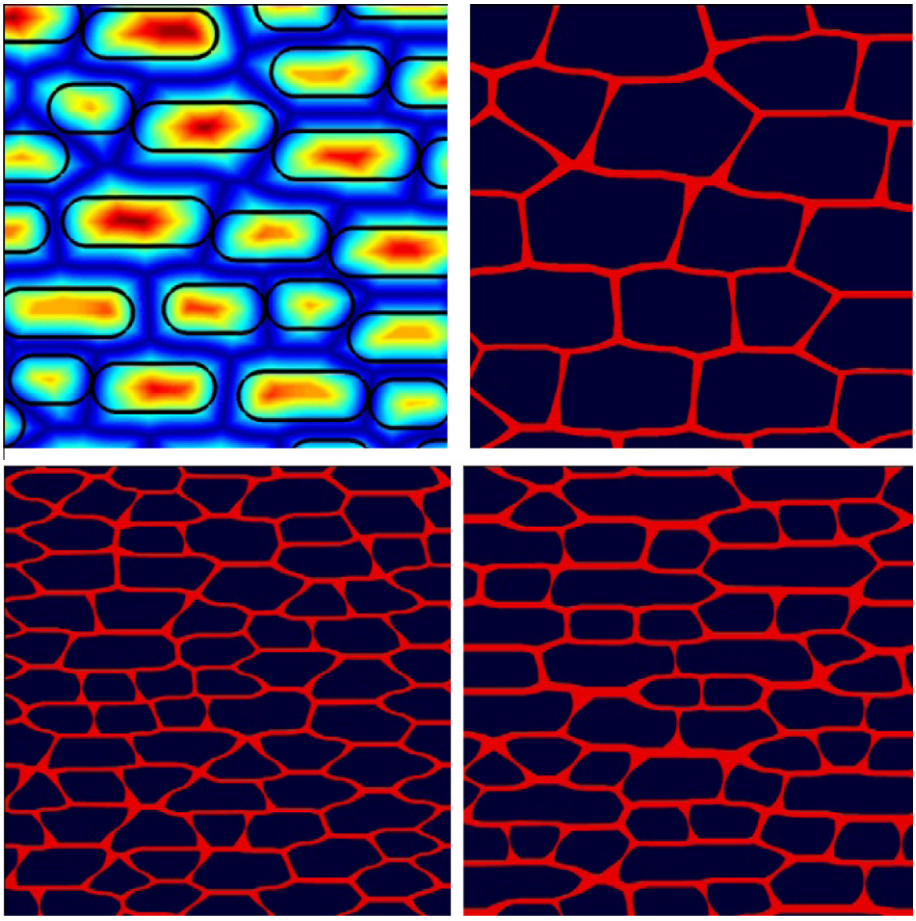

Fig. 30. Generation of old masonry RVEs (top-left) Initial elongated and oriented inclusion distribution. $LS_1(\mathbf{x}) - LS_2(\mathbf{x})$. γ shown in background is used to extract curves for natural rocks geometry. (top right) Extracted geometry with (12), $\gamma = 1.2$ and $t = 0.005$. (Bottom) Random generation of other periodic RVEs.

shape can be determined independently in either space. This could result in achieving dense packing of elongated and globally orientated particles.

- *Intermediate methods*. Value of $LS_2(\mathbf{x})$ at any $\mathbf{x}$ on $LS_1(\mathbf{x}) = 0$ may be used to construct a force field acting on inclusions in the RVE depending on local inclusion inter-distances. This information could subsequently be used to steer a computationally cheap DEM manipulation in order to increase the density or modify the RVE.

Finally, it is emphasized that the present method is made of independent tools, and can be used in correlation with other methods. More particularly, the LS-RSA inclusion distribution generator, although being more efficient than a classical RSA, may be completed by a suited DEM simulation in order to generate RVEs with given microstructural features resulting from a dynamic process or even to simply increase the density of the packing. However, it is believed that the presented framework has a clear added value in the following four types of situations.

- When coupled with a XFEM mechanical implementation, it may be combined as a "all in one" framework for broad multi-scale studies, allowing the generation of large numbers of RVEs with all parametric variations desired, directly usable in a mechanical or coupled computation. Since XFEM based techniques using level set descriptions allow uncoupling the discretisation from the material boundaries, such a combined framework would allow reducing dramatically the analyst time required for such investigations.
- The LS-RSA tool can also be used in stand-alone, as a pre-processing tool for DEM-based methods, since it offers packing possibilities that are out of reach for classical RSA approaches.
- For more specific arrangements, such as very close packing of rocks or polycrystalline microstructures, the proposed methodology brings an alternative RVE generation tool that broadens the scope of RVEs that can be generated, in particular with a strong control on the size distribution of inclusions.
- Finally, the proposed method allows the incorporation of a third specific (bridging) phases in the RVE for specific fabric reproduction.

7. Conclusion and future prospects

A new RVE generation tool was presented based on the concept of level set. The proposed methodology rests on an extension of classical Random Sequential Addition approaches combined with a level set function control on the random addition process. Based on level set functions used as distance indicators, the random addition process of RSA can be dramatically optimized. In particular, the exponentially increasing computational cost of the addition process is turned into a cost that linearly depends on the number of inclusions to add in the RVE generation. Nearest neighbor and second nearest neighbor conditions on the addition process can be performed at no extra additional cost.

For complex microstructures generation, the level set control allows in addition considering modifications in the inclusion shapes (morphing) in an efficient way, which permits a further increase of the density of the obtained packings. The level set formal-

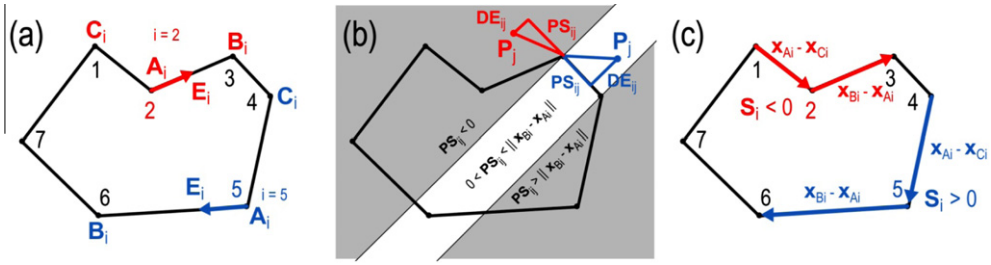

Fig. 31. Geometrical definitions and relations used in the presented algorithm.

ism was also shown to allow the incorporation of a third bridging phase between the added inclusions, enabling the generation of 3 phases systems, a result difficult to achieve with concurrent methods.

The performance of the proposed framework was assessed, showing that complex RVEs can be obtained very efficiently with high packing densities, especially with broad size distributions. Its application was illustrated on various examples of different physical natures, e.g. computational generation of microstructures for soils incorporating particles and a bridging clay phase, for polycrystals with bimodal grain size distributions, and for masonry. In spite of this variety of applications, it is emphasized that the related RVEs are all generated within the proposed unified level set controlled framework.

Some points can be pointed as future desirable work. First, the incorporation of elongated or strongly non convex inclusions could be considered, as mentioned in the discussion section. Next, the presented principles may be straightforwardly extended to generate 3D RVEs which may be needed in applications for the purpose of experimental comparisons. The exploitation of the generated RVEs in mechanical computations coupled to XFEM discretisation techniques or FFT-based homogenization methods is a next development step as well, in situations in which the classical FEM approach is subjected to major difficulties at the meshing stage.

Acknowledgements

The authors would like to thank Prof. L.J. Sluys and Dr. M. Stroeven from TUDelft for fruitful interactions and discussions.

Appendix A. Level set for 2D polygonal interfaces

The distance from a point to a polygon (convex or not) is the minimum of distances from this point to each vertices and edges of the polygon. We denote **P** a set of j point in the RVE for which a value of the polygon Level Set has to be evaluated and **A** the set of vertices v_i of the polygon, i listing vertices in clockwise order. Sets **B** and **C** are constructed from **A** such as the first vertex in **A** become the last in **B**, and the last in **A** become the first in **C**. Hence, for a given i, $\mathbf{A}_i$ is the vertex i, $\mathbf{B}_i$ is the next one in clockwise order and $\mathbf{C}_i$ is the previous one in clockwise order. See Fig. 31a for an example in which $\mathbf{A}_i$, $\mathbf{B}_i$ and $\mathbf{C}_i$ are illustrated for $i = 2$ and 5. Under such condition, the following relations can be written:

The distance between each $\mathbf{P}_j$ and each $\mathbf{A}_i$ is given by

$$\mathbf{DV}_{ij} = \|\mathbf{x}_{Pj} - \mathbf{x}_{Ai}\|. \tag{A.1}$$

Each edge $\mathbf{A}_i\mathbf{B}_i$ direction is defined by (see Fig. 31a)

$$\mathbf{E}_i = (\mathbf{x}_{Bi} - \mathbf{x}_{Ai})/\|\mathbf{x}_{Bi} - \mathbf{x}_{Ai}\|. \tag{A.2}$$

The distance between each $\mathbf{P}_j$ and each $\mathbf{A}_i\mathbf{B}_i$ edge is given by (see Fig. 31b)

$$\mathbf{DE}_{ij} = \|\mathbf{E}_i \times (\mathbf{x}_{Pj} - \mathbf{x}_{Bi})\|. \tag{A.3}$$

But is restricted to the area defined by (see Fig. 31b)

$$0 < \mathbf{PS}_{ij} = \|\mathbf{E}_i \cdot (\mathbf{x}_{Pj} - \mathbf{x}_{Bi})\| > \|\mathbf{x}_{Bi} - \mathbf{x}_{Ai}\|. \tag{A.4}$$

Finally, the concavity of each vertices $\mathbf{A}_i$ is given by (see Fig. 31c)

$$\mathbf{S}_i = \text{sign}[(\mathbf{x}_{Bi} - \mathbf{x}_{Ai}) \times (\mathbf{x}_{Ai} - \mathbf{x}_{Ci})] \tag{A.5}$$

The algorithm to evaluate LS($\mathbf{P}_j$) is the following:

- Compute $\mathbf{DV}_{ij}$ and $\mathbf{DE}_{ij}$.
- For each $\{i,j\}$ which does not satisfy relation (A.4), replace $\mathbf{DE}_{ij}$ by $+\infty$.
- For each j choose the minimum of ($\mathbf{DV}_{ij} \cup \mathbf{DE}_{ij}$).
- Set the sign for each retained value, values coming from $\mathbf{DV}_{ij}$ are negatives if corresponding $\mathbf{S}_i$ are negatives and values coming from $\mathbf{DE}_{ij}$ are negative if the z component of the corresponding vector product in the relation (A.3) are negative.

References

[1] G. Abrivard, E.P. Busso, G. Cailletaud, S. Forest, Modeling of Deformation of FCC Polycrystalline Aggregates Using a Dislocation-based Crystal Plasticity Model, AIP Conf. Proc. 908 (2007) 661–666.
[2] D. Adalsteinsson, J.A. Sethian, A fast level set method for propagating interface, J. Comput. Phys. 118 (1995) 269–277.
[3] K.E. Aifantis, A.A. Konstantinidis, Hall–Petch revisited at the nanoscale, Mater. Sci. Eng. B 163 (2009) 139–144.
[4] R. Al-Raoush, M. Alsaleh, Simulation of random packing of polydisperse particles, Powder Technol. 176 (2007) 47–53.
[5] J. E Andrade, C.F. Avila, S.A. Hall, N. Lenoir, G. Viggiani, Multiscale modeling and characterization of granular matter: from grain kinematics to continuum mechanics, J. Mech. Phys. Solids 59 (2011) 237–250.
[6] F. Barbe, S. Forest, G. Cailletaud, Intergranular and intragranular behavior of polycrystalline aggregates. Part 2: Results, Int. J. Plasticity 17 (2001) 537–563.
[7] F. Bouchelaghem, A. Benhamida, H. Quoc Vu, Nonlinear mechanical behaviour of cemented soils, Comput. Mater. Sci. 48 (2010) 287–295.
[8] A.V. Bui, R. Manasseh, K. Liffman, I.D. Sutalo, Development of optimized vascular fractal tree models using level set distance function, Med. Engrg. Phys. 32 (2010) 790–794.
[9] P. Bullock, N. Fedoroff, A. Jongerius, G. Stoops, T. Tursina, U. Babel, Handbook for Soil Thin Section Description, Cambridge University Press, New York, 1999.
[10] N. Chernov, Y. Stoyan, T. Romanova, Mathematical model and efficient algorithms for object packing problem, Comput. Geom. 43 (2010) 535–553.
[11] D. Coelho, J.-F. Thovert, P.M. Alder, Geometrical and transport properties of random packing of spheres and a spherical particles, Phys. Rev. E 55 (1997) 1959–1978.
[12] D.W. Cooper, Random-sequential-packing simulations in three dimensions for spheres, Phys. Rev. A 38 (1988) 522–524.
[13] P.A. Cundall, O.D.L. Strack, A discrete numerical model for granular assemblies, Géotechnique 29 (1979) 47–65.
[14] P.A. Cundall, Formulation of a three-dimensional distinct element model—Part I. A scheme to detect and represent contacts in a system composed of many polyhedral blocks, Int. J. Rock Mech. Mining Sci. Geomech. 25 (1988) 107–116.
[15] P.A. Cundall, Formulation of a three-dimensional distinct element model—Part II. Mechanical calculations for motion and interaction of a system composed of many polyhedral blocks, Int. J. Rock Mech. Mining Sci. Geomech. 25 (1988) 117–125.
[16] R. De Bel, J.C. Verbrugge, A. Gomes Correia, Comportamento geomecânico de solos estabilizados com cal. Principais contribuiçoes do projecto COGESTAC – Geomechanical behaviour of stabilized soils with lime; the main contributions of COGESTAC, in: 12th Congresso Nacional de Geotecnica, Guimaraes, 2010.
[17] D. Deganello, A.J. Williams, T.N. Croft, A.S. Lubansky, D.T. Gethin, T.C. Claypole, Level-set method for the modelling of liquid bridge formation and break-up, Comput. Fluids 40 (2011) 42–51.

[18] K. Dréau, N. Chevaugeon, N. Moës, Studied X-FEM enrichment to handle material interfaces with higher order finite element, Comput. Methods Appl. Mech. Engrg. 199 (2010) 1922–1936.
[19] F. Feyel, J.-L. Chaboche, FE2 multiscale approach for modelling the elastoviscoplastic behaviour of long fibre SiC/Ti composite materials, Comput. Methods Appl. Mech. Engrg. 183 (2000) 309–330.
[20] B. François, C. Dascalu, A two-scale time-dependent damage model based on non-planar growth of micro-cracks, J. Mech. Phys. Solids 58 (2010) 1928–1946.
[21] G. Fu, W. Dekelbab, 3-D random packing of polydisperse particles and concrete aggregate grading, Powder Technol. 133 (2003) 147–155.
[22] I.M. Gitman, H. Askes, L.J. Sluys, Representative volume: existence and size determination, Engrg. Fract. Mech. 74 (2007) 2518–2534.
[23] T. Hettich, E. Ramm, Interface material failure modeled by the extended finite-element method and level sets, Comput. Methods Appl. Mech. Engrg. 195 (2006) 4753–4767.
[24] T. Hettich, A. Hund, E. Ramm, Modeling of failure in composites by X-FEM and level sets within a multiscale framework, Comput. Methods Appl. Mech. Engrg. 197 (2008) 414–424.
[25] H. He, Computational modelling of particle packing in concrete, Ph.D. Thesis, Delft University of Technology, The Netherlands, 2010.
[26] H. He, Z. Guo, P. Stroeven, M. Stroeven, L.J. Sluys, Strategy on simulation of arbitrary-shaped cement grains in concrete, Image Anal. Stereol. 29 (2010) 79–84.
[27] B. Hiriyur, H. Waisman, G. Deodatis, Uncertainty quantification in homogenization of heterogeneous microstructures modeled by XFEM, Int. J. Numer. Methods Engrg. (2011), http://dx.doi.org/10.1002/nme.3174.
[28] S.J. Hollister, N. Kikuchi, Homogenization theory and digital imaging: a basis for studying the mechanics and design principles of bone tissue, Biotechnol. Bioeng. 43 (1994) 586–596.
[29] X. Jia, R.A. Williams, A packing algorithm for particles of arbitrary shapes, Powder Technol. 120 (2001) 175–186.
[30] X. Jia, R.A. Williams, D. Rhodes, Validation of a digital packing algorithm in predicting powder packing densities, Powder Technol. 174 (2007) 10–13.
[31] S. -M Kim, R.K. Abu Al-Rub, Meso-scale computational modeling of the plastic–damage response of cementitious composites, Cement Concr. Res. 41 (2011) 339–358.
[32] R. Kimmel, A. Bruckstein, Shape offsets via level sets, Comput. Aided Des. 25 (1993) 154–162.
[33] V. Kousnetsova, W.A.M. Brekelmans, F.T.P. Baaijens, An approach to micro–macro modeling of heterogeneous materials, Comput. Mech. 27 (2001) 37–48.
[34] V. Kouznetsova, M.G.D. Geers, W.A.M. Brekelmans, Multi-scale constitutive modelling of heterogeneous materials with a gradient-enhanced computational homogenization scheme, Int. J. Numer. Methods Engrg. 54 (2002) 1235–1260.
[35] G. Legrain, P. Cartraud, I. Perreard, N. Moës, An X-FEM and level set computational approach for image-based modeling: Application to homogenization, Int. J. Numer. Methods Engrg. 86 (2011) 915–934.
[36] S. Liu, Z. Ha, Prediction of random packing limit for multimodal particle mixtures, Powder Technol. 126 (2002) 283–296.
[37] M. Lombardo, J. Zeman, M. Sejnoha, G. Falsone, Stochastic modeling of chaotic masonry via mesostructural characterization, Int. J. Multiscale Comput. Engrg. 7 (2009) 171–185.
[38] R. Malladi, J.A. Sethian, B.C. Vemuri, Shape modeling with front propagation: a level set approach, IEEE Trans. Pattern Anal. Mach. Intell. 17 (1995) 158–175.
[39] R. Masson, M. Bornet, P. Suquet, A. Zaoui, An affine formulation for the prediction of the effective properties of nonlinear composites and polycrystals, J. Mech. Phys. Solids 48 (2000) 1203–1227.
[40] T.J. Massart, R.H.J. Peerlings, M.G.D. Geers, Mesoscopic modeling of failure and damage-induced anisotropy in brick masonry, Eur. J. Mech. A/Solids 23 (2004) 719–735.
[41] T.J. Massart, R.H.J. Peerlings, M.G.D. Geers, A dissipation-based control method for the multi-scale modelling of quasi-brittle materials, CR Mec. 333 (2005) 521–527.
[42] T.J. Massart, R.H.J. Peerlings, M.G.D. Geers, Structural damage analysis of masonry walls using computational homogenization, Int. J. Damage Mech. 16 (2007) 199–226.
[43] T.J. Massart, T. Pardoen, Strain gradient plasticity analysis of the grain-size-dependent strength and ductility of polycrystals with evolving grain boundary confinement, Acta Mater. 58 (2010) 5768–5781.
[44] B.C.N. Mercatoris, P. Bouillard, T.J. Massart, Multi-scale detection of failure in planar masonry thin shells using computational homogenisation, Engrg. Fract. Mech. 76 (2009) 479–499.
[45] B.C.N. Mercatoris, T.J. Massart, A coupled two-scale computational scheme for the failure of periodic quasi-brittle thin planar shells and its application to masonry, Int. J. Numer. Methods Engrg. 85 (2011) 1177–1206.
[46] J.C. Michel, H. Moulinec, P. Suquet, Effective properties of composite materials with periodic microstructure: a computational approach, Comput. Methods Appl. Mech. Eng. 172 (1999) 109–143.
[47] C. Miehe, J. Dettmar, A framework for micro–macro transitions in periodic particle aggregates of granular materials, Comput. Methods Appl. Mech. Engrg. 193 (2004) 225–256.
[48] G. Milani, P.B. Lourenço, A. Tralli, Homogenised limit analysis of masonry walls. Part I: Failure surfaces, Comput. Struct. 84 (2006) 166–180.
[49] G. Milani, P.B. Lourenço, Monte Carlo homogenized limit analysis model for randomly assembled blocks in-plane loaded, Comput. Mech. 46 (2010) 827–849.
[50] G. Milani, D. Benasciutti, Homogenized limit analysis of masonry structures with random input properties: polynomial response surface approximation and Monte Carlo simulations, Struct. Engrg. Mech. 34 (2010) 417–447.
[51] N. Moës, M. Cloirec, P. Cartraud, J-F. Remacle, A computational approach to handle complex microstructure geometries, Comput. Methods Appl. Mech. Engrg. 192 (2003) 3163–3177.
[52] H. Moulinec, P. Suquet, A fast numerical method for computing the linear and nonlinear properties of composites, CR Acad. SC. Paris II 318 (1994) 1417–1423.
[53] H. Moulinec, P. Suquet, A numerical method for computing the overall response of nonlinear composites with complex microstructure, Comput. Methods Appl. Mech. Engrg. 157 (1998) 69–94.
[54] A. Musienko, A. Tatschl, K. Schmidegg, O. Kolednik, R. Pippan, G. Cailletaud, Three-dimensional finite element simulation of a polycrystalline copper specimen, Acta Mater. 55 (2007) 4121–4136.
[55] V.P. Nguyen, O.L. Valls, M. Stroeven, L.J. Sluys, On the existence of representative volumes for softening quasi-brittle materials – a failure zone averaging scheme, Comput. Methods Appl. Mech. Engrg. 199 (2010) 3028–3038.
[56] S. Osher, R. Fedkiw, Level Set Methods and Dynamic Implicit Surfaces, Springer-Verlag, New York, 2002.
[57] S. Osher, J.A. Sethian, Fronts propagating with curvature-dependent speed: algorithms based on Hamilton–Jacobi formulations, J. Comput. Phys. 79 (1988) 12–49.
[58] P.-O. Persson, Mesh generation for implicit geometries, Ph.D. Thesis, Massachusetts, 2005.
[59] O. Pierard, C. Friebel, I. Doghri, Mean field homogenization of multi phase thermo-elastic composites: a general framework and its validation, Compos. Sci. Technol. 64 (2004) 1587–1603.
[60] H. Qing, L. Mishnaevsky Jr., 3D hierarchical computational model of wood as a cellular material with fibril reinforced, heterogeneous multiple layers, Mech. Mater. 41 (2009) 1034–1049.
[61] D. Raabe, M. Sachtleber, Z. Zhao, F. Roters, S. Zaefferer, Micromechanical and macromechanical effects in grain scale polycrystal plasticity: experimentation and simulation, Acta Mater. 49 (2001) 3433–3441.
[62] H. Resk, L. Delannay, M. Bernacki, T. Coupez, R. Logé, Adaptive mesh refinement and automatic remeshing in crystal plasticity finite element simulations, Modell. Simul. Mater. Sci. Engrg. 17 (2009) 75012–75022.
[63] H. Sadouki, F.H. Wittmann, On the analysis of the failure process in composite materials by numerical simulation, Mater. Sci. Engrg. 104 (1988) 9–20.
[64] S. Sankaran, N. Zabaras, Computing property variability of polycrystals induced by grain size and orientation uncertainties, Acta Mater. 55 (2007) 2279–2290.
[65] E. Sanchez-Palencia, Non-homogeneous media and vibration theory, Lect. Notes Phys. 127 (1980).
[66] I. Saxl, P. Ponizil, Grain size estimation: w–s diagram, Mater. Charact. 46 (2001) 113–118.
[67] I. Saxl, P. Ponizil, Bernoulli cluster field: Voronoi tessellations, Appl. Math. 47 (2002) 157–167.
[68] K.L. Scrivener, A.K. Crumbie, P. Laugesen, The interfacial transition zone (ITZ) between cement past and aggregate in concrete, Interface Sci. 12 (2004) 411–421.
[69] J. Sejnoha, M. Sejnoha, J. Zeman, J. Sykora, J. Vorel, Mesoscopic study on historic masonry, Struct. Engrg. Mech. 30 (2009) 99–117.
[70] J.A. Sethian, Evolution, implementation, and application of level set and fast marching methods for advancing fronts, J. Comput. Phys. 169 (2001) 503–555.
[71] J.A. Sethian, Level Set Methods and Fast Marching Methods, Cambridge University Press, New York, 1999.
[72] J.D. Sherwood, Packing of spheriods in three-dimensional space by random sequential addition, J. Phys. A 30 (1997) 839–843.
[73] D.S. Stafford, T.L. Jackson, Using level sets for creating virtual random packs of non-spherical convex shapes, J. Comput. Phys. 229 (2010) 3295–3315.
[74] M. Stroeven, H. Askes, L.J. Sluys, Numerical determination of representative volumes for granular materials, Comput. Methods Appl. Mech. Engrg. 193 (2004) 3221–3238.
[75] P. Stroeven, L.J. Sluys, Z. Guo, M. Stroeven, Virtual reality studies of concrete, Forma 21 (2006) 227–242.
[76] P. Stroeven, H. He, Z. Guo, M. Stroeven, Particle packing in a model concrete at different levels of the microstructure: evidence of an intrinsic patchy nature, Mater. Charact. 60 (2009) 1088–1092.
[77] M. Stroeven, P. Stroeven, SPACE system for simulation of aggregated matter application to cement hydration, Cem. Concr. Res. 29 (1999) 1299–1304.
[78] M. Stroeven, Discrete numerical modelling of composite materials – application to cementitious materials, Ph.D. Thesis, Delft, 1999.
[79] J.W. Suh, D. Scheinost, D.P. Dione, L.W. Dobrucki, A.J. Sinusas, A non-rigid registration method for serial lower extremity hybrid SPECT/CT imaging, Med. Image Anal. 15 (2011) 96–111.
[80] N. Sukumar, D.L. Chopp, N. Moës, T. Belytschko, Modeling holes and inclusions by level sets in the extended finite-element method, Comput. Methods Appl. Mech. Engrg. 190 (2001) 6183–6200.
[81] V. Sundararaghavan, N. Zabaras, Design of microstructure-sensitive properties in elasto-viscoplastic polycrystals using multi-scale homogenization, Int. J. Plasticity 22 (2006) 1799–1824.
[82] J. Talbot, P. Schaaf, G. Tarjus, Random sequential addition of hard spheres, Mol. Phys. 72 (1991) 1397–1406.

[83] K. Terada, M. Hori, T. Kyoya, N. Kikuchi, Simulation of the multi-scale convergence in computational homogenization approaches, Int. J. Solids Struct. 37 (2000) 2285–2311.
[84] A. Tewari, A.M. Gokhale, Nearest-neighbor distances between particles of finite size in three-dimensional uniform random microstructures, Mater. Sci. Engrg. 385 (2004) 332–341.
[85] A.B. Tran, Q.-C. He, C. Toulemonde, J. Sanahuja, A multiple level set approach to prevent numerical artefacts in complex microstructures with nearby inclusions within XFEM, Int. J. Numer. Methods Engrg. 85 (2011) 1436–1459.
[86] T. Xu, M. Li, Topological and statistical properties of a constrained Voronoi tessellation, Philos. Mag. 89 (2009) 349–374.
[87] O.U. Uche, F.H. Stillinger, S. Torquato, Concerning maximal packing arrangements of binary disk mixtures, Physica A 342 (2004) 428–446.
[88] O. van der Sluis, P.H.J. Vosbeek, P.J.G. Schreurs, H.E.H. Meijer, Homogenization of heterogeneous polymers, Int. J. Solids Struct. 36 (1999) 3193–3214.
[89] Y.M. Wang, E. Ma, Three strategies to achieve uniform tensile deformation in a nanostructured metal, Acta Mater. 52 (2004) 1699–1709.
[90] S.Y. Wang, K.M. Lim, B.C. Khoo, M.Y. Wang, An extended level set method for shape and topology optimization, J. Comput. Phys. 221 (2007) 395–421.
[91] C. Wellmann, C. Lillie, P. Wriggers, Homogenization of granular material modeled by a three-dimensional discrete element method, Comput. Geotech. 35 (2008) 394–405.
[92] S.R. Williams, A.P. Philipse, Random packings of spheres and spherocylinders simulated by mechanical contraction, Phys. Rev. E 67 (2003) 1–9.
[93] X. Xie, M. Mirmehdi, Radial basis function based level set interpolation and evolution for deformable modelling, Image Vis. Comput. 29 (2011) 167–177.
[94] J. Zeman, M. Sejnoha, From random microstructures to representative volume elements, Modell. Simul. Mater. Sci. Engrg. 15 (2007) 325–335.
[95] A.M. Zsaki, An efficient method for packing polygonal domains with disks for 2D discrete element simulation, Comput. Geotech. 36 (2009) 568–576.